3D bioprinting of bioproduction cell lines

Laura Chastagnier, Lucie Essayan, Celine Thomann, Julia Niemann, Elisabeth Errazuriz-Cerda, Manon Laithier, Anne Baudouin, Christophe Marquette, Emma Petiot

Bioprinting

Bioproduction Cell lines 3D bioprinting

--Manuscript Draft--

Manuscript Number:	
Article Type:	Research paper
Keywords:	3D Bioprinting; 3D Cell proliferation; Metabolic activity; Hydrogel microporosity; Bioproduction cell lines

Corresponding Author:	Emma Petiot, PHD Institute of Molecular and Supramolecular Chemistry and Biochemistry FRANCE
First Author:	Laura Chastagnier
Order of Authors:	Laura Chastagnier
	Lucie Essayan
	Celine Thomann
	Julia Niemann
	Elisabeth Errazuriz-Cerda
	Manon Laithier
	Anne Baudouin
	Christophe Marquette
	Emma Petiot, PHD

Abstract:	Three-dimensional (3D) bioprinting presents a transformative approach to replicating vivo-like environments for mammalian cell cultures, offering potential advances in bioproduction and tissue engineering. In this study, we investigated the growth, metabolic activity, and structural organization of four mammalian cell lines (HEK, MDCK, CHO, and Vero) in 3D bioprinted constructs. Our results demonstrate that even highly selected, immortalised cell lines can regain physiological traits closer to their native tissue when cultured in 3D environments. We observed significant shifts in proliferation kinetics, including reduced growth rates and reduced fermentative activity. A Design of Experiment (DOE) approach identified critical biofabrication parameters—such as hydrogel microporosity and consolidation conditions—that modulate cell behavior and proliferation in 3D matrices. These findings highlight the potential of 3D bioprinting not only for medical applications, such as regenerative medicine and drug testing, but also for enhancing bioproduction processes by supporting higher cell densities and metabolic efficiency. Our work underscores the importance of optimizing 3D culture conditions to mimic vivo-like behaviors and improve productivity, offering new insights into the scalability of bioprinted constructs for industrial applications.

Opposed Reviewers:	

Emma PETIOT, PhD
Scientist CNRS
Quality Assurance Manager 3d.FAB platform
Director 3D InnovationLab joint laboratory 3d.FAB / Sartorius
3d.FAB platform
Gembas Team - ICBMS laboratory - Bat Lederer - 1 rue Victor Grignard - Campus LyonTech/la Doua
43, boulevard du 11 Novembre 1918 - BP 82077 - 69 616 VILLEURBANNE Cedex
Phone: (0)6 47 60 59 13

17 janvier 2025

Dear Editor of *Bioprinting*,

Please find enclosed our original work entitled “Bioproduction Cell Lines 3D Bioprinting,” which we would like you to consider for publication in *Bioprinting*.

In this study, we investigate and quantify the physiological changes occurring when bioproduction cell lines are cultivated in a 3D bioprinted environment. We further identify key biofabrication parameters that influence these physiological changes using a design of experiment approach coupled with Partial Least Square analysis. As bioprinting is the only biofabrication tool that enables the reproducible, controllable, and scalable generation of 3D cellularized constructs, we bioprinted four distinct cell lines within an in-house developed biocompatible and proliferative hydrogel. The proliferation and metabolic behavior of these cells were then thoroughly characterized. A final aspect of our study explores how tuning the hydrogel composition can enhance cell proliferation and recovery of physiological behaviors, thereby optimizing the bioproduction process.

This work provides novel quantitative insights into the metabolic and proliferative adaptations of bioprinted cell cultures, filling a crucial gap in the literature. Furthermore, our findings present compelling prospects for the use of bioprinting in bioproduction, particularly for therapeutic and vaccine development. Traditional bioproduction cell lines have long been cultivated in 2D or suspension cultures; our research explores the advantages of 3D cultures, where cells can densely colonize a volume while exhibiting metabolic adaptations that may favor biomolecule production or viral infection. Additionally, the 3D bioprinted constructs offer enhanced protection from hydrodynamic shear stress caused by media stirring and gas bubbles, which can be detrimental in standard bioproduction settings.

We believe that our findings align well with the scope of *Bioprinting* and will be of interest to its readership. We appreciate your time and consideration and look forward to the opportunity to contribute to your esteemed journal.

Best regards,

Emma PETIOT, PhD

Bioproduction Cell lines 3D bioprinting

Laura Chastagnier [1], Lucie Essayan[1], Celine Thomann[1], Julia Niemann[3], Elisabeth Errazuriz-Cerda[4], Manon Laithier[1;2], Anne Baudouin[2], Christophe Marquette[1], Emma Petiot*[1]

[1] 3d.FAB, Univ Lyon, Université Lyon1, CNRS, INSA, CPE-Lyon, ICBMS, UMR 5246, 43, Bd du 11 novembre, 69100 Villeurbanne cedex, France
[2] Centre Commun de RMN, CNRS, Université Lyon 1, CPE-Lyon, Bâtiment Lederer, 1 Rue Victor Grignard, 69100 Villeurbanne, France
[3] Sartorius Stedim Biotech Gmbh, August Spindler Strasse 11 Goettingen, D-37079 Germany
[4] Centre d'Imagerie Quantitative Lyon-Est (CIQLE), Université Claude Bernard Lyon 1, Lyon, France

Corresponding author : emma.petiot@univ-lyon1.fr

Emma PETIOT ORCID : 0000-0002-1989-4695

ABSTRACT

Three-dimensional (3D) bioprinting presents a transformative approach to replicating vivo-like environments for mammalian cell cultures, offering potential advances in bioproduction and tissue engineering. In this study, we investigated the growth, metabolic activity, and structural organization of four mammalian cell lines (HEK, MDCK, CHO, and Vero) in 3D bioprinted constructs. Our results demonstrate that even highly selected, immortalised cell lines can regain physiological traits closer to their native tissue when cultured in 3D environments. We observed significant shifts in proliferation kinetics, including reduced growth rates and reduced fermentative activity. A Design of Experiment (DOE) approach identified critical biofabrication parameters—such as hydrogel microporosity and consolidation conditions—that modulate cell behavior and proliferation in 3D matrices. These findings highlight the potential of 3D bioprinting not only for medical applications, such as regenerative medicine and drug testing, but also for enhancing bioproduction processes by supporting higher cell densities and metabolic efficiency. Our work underscores the importance of optimizing 3D culture conditions to mimic vivo-like behaviors and improve productivity, offering new insights into the scalability of bioprinted constructs for industrial applications.

KEYWORDS

3D Bioprinting, 3D Cell proliferation, Metabolic activity, Hydrogel microporosity, Bioproduction cell lines.

1 INTRODUCTION

In vitro cell culture allows the growth of cells in an artificial environment to study their characteristics and functions. Cells have been cultured on flat, 2D surfaces for studying diseases and testing drugs for many years. This method is popular due to its simplicity, homogeneity, and minimal uncontrolled variables, making it easy to use. However, 2D cultures fail to accurately represent in vivo mechanisms (Anton et al., 2015; Hutchinson and Kirk, 2011). Over the past few decades, attention has shifted toward 3D cell cultures, which more closely mimic the in vivo environment (Ravi et al., 2015; Souza et al., 2018a). This approach is particularly valuable in research on tissue regeneration, cell signalling, cell interaction and disease modelling, and drug testing, as it allows for more complex interactions. However, it is more technically challenging, with a greater number of uncontrolled factors affecting cell behavior. As examples, cell-cell and cell-matrix interactions, mediated by integrins and cadherins, play key roles in cellular signaling and function in 3D environments (Hynes, 2002; Klezovitch and Vasioukhin, 2015; Martinac et al., 2020). Cell behaviour and differentiation is then affected by 3D support nature (Chagnon-Lessard et al., 2021; Guo et al., 2014; Kawaue et al., 2023), porosity and micro-pattern (Moussa et al., 2018) as well as its mechanical properties (Martinac et al., 2020; Mih et al., 2012). The interactions between cells and the extracellular matrix in 3D environments, along with the restricted diffusion of nutrients, waste, or drugs, are known to influence the expression of various genes, including those involved in regulating cell proliferation, apoptosis, survival, and differentiation. Despite these advances, detailed descriptions of physiological changes, particularly in cell proliferation rates and central carbon metabolism, in 3D cultures remain limited. This gap in knowledge is likely due to the absence of precise data on metabolic fluxes and rates in primary cells. In contrast, the pharmaceutical industry has accumulated extensive data on the proliferation and metabolism of various immortalized cell lines, particularly in 2D and suspension cultures. Biopharmaceutical production from animal cell lines has been developed since the 1980s, enabling the production of many therapeutic proteins and viruses at industrial scales (Kuystermans and Al-Rubeai, 2015). Over decades, cell lines have been optimized to enhance productivity. These animal cell lines have been selected and adapted to maximize bioproduction yields for decades. They are immortalized, highly selected or mutated, and present non-physiological behaviors (Reinhart et al., 2019; Yuan et al., 2018). Their growth, death and metabolic kinetics were extensively described with precise Flux Balance Analysis (FBA) (Bastin et al., 2021; Martínez et al., 2013; Martínez-Monge et al., 2019; Wahl et al., 2008;

Zamorano et al., 2010) and vast databases describing their biological kinetics are available. Such deep understanding of production cell line behaviors was mandatory to optimize biopharmaceutical production processes.

In our study, we focus on physiological changes in four well-established production cell lines—HEK, MDCK, CHO, and Vero—grown in 3D environment. These cell lines are widely used in biopharmaceutical research and production. CHO cells, for example, are the leading platform for producing monoclonal antibodies, with 89% of approved mammalian-cell-based products derived from them (Walsh and Walsh, 2022). HEK293 cells are frequently used to produce recombinant proteins and viral vectors (Agarwal et al., 2020). Increasing production capacity is now focused on cell densification as well as cell feeding strategies (Fed-batch / perfusion) (Schulze et al., 2021). On the counterpart, cell physiology and intrinsic secretion capacity is explored only with a genome editing point of view.

We propose exploring a new approach by introducing 3D culture techniques for production cell lines. We believe that gaining insights into the physiological differences associated with 3D cell cultures could offer innovative perspectives for bioproduction applications. Notably, recent studies have reported enhancements in the production capabilities of cell lines when cultivated in 3D environments (Wong et al., 2007). This research aims to bridge the knowledge gap between conventional 2D culture / suspension systems and the more complex, but promising, 3D environments. Our goal is to advance both fundamental biological understanding and potential further industrial applications. Specifically, we aim to describe the growth capacity, central carbon metabolism kinetics, and 3D cell organization of four production cell lines, marking a significant step in understanding and quantifying the physiological changes that occur in 3D cultures. For the biofabrication process, microextrusion 3D bioprinting was chosen. Over the past decade, this method has become a pivotal tool in 3D biofabrication. Its advantages include uniform and reproducible cell distribution (Matai et al., 2020), the ability to create intricated and controlled 3D structures (Pourchet et al., 2017), and scalability (Matai et al., 2020). Extensive preliminary studies also demonstrated the ability to support growth of several primary and continuous cell lines (Marquette et al., 2024). Thus, the final part of our work focuses on identifying biofabrication parameters, such as scaffold composition and printing conditions, that influence 3D cellular kinetics using a design-of-experiment (DoE) approach.

2 MATERIAL AND METHODS

2.1 Cell culture

The experiments were performed using HEK293T cells kindly provided by Dr. C. Maisse-Paradisi (INRA-UCBL-EPHE "Viral Infections and Comparative Pathology," Lyon, France), CHO DG44 (PTN1-CB-CC1; Cellca-Sartorius), MDCK (VirPath – CIRI - U1111 INSERM - UMR 5308 CNRS - ENS Lyon - UCBL1) and Vero (CCL-81™; ATCC®). HEK, MDCK, CHO, and Vero were cultured in Dulbecco's Modified Eagle Medium (DMEM, Gibco, Thermo Fisher Scientific, Etats-Unis, 31966-021) supplemented with 10% (v/v) FBS (Gibco Cell Culture, 10270-106). This report will refer to this culture medium as DMEM(+). The cells were amplified before bioprinting experiments in T75 flasks (Corning) in a standard incubator (5% CO2, 80% humidity at 37°C).

2.2 Formulation, Bioprinting, and Consolidation of Cellularized Bioink

The bioink was prepared by mixing Fibrinogen, Alginate, and Gelatin in calcium-free DMEM (Thermofisher, 21068028) supplemented with 10% FBS (Thermofisher scientific, A3160), 250 U/mL Penicillin/Streptomycin (15140122, GIBCO), and 5 µg/mL Amphotericin B (15290026, GIBCO). Two formulations were used: Formulation A (2% w/v Fibrinogen, 2% w/v Alginate, 5% w/v Gelatin) and Formulation B (2% w/v Fibrinogen, 1% w/v Alginate, 10% w/v Gelatin). Cells at concentrations of 1.0×10^6 or 3.0×10^6 cells/mL were mixed with the bioink, homogenized, and loaded into sterile syringes, followed by a 30-minute incubation at 21°C for Formulation A or 28°C for Formulation B. Bioprinting was performed using a BioAssemblyBot 3D printer (Advanced Solution, Inc) with pneumatic extrusion at pressures of 20-50 psi, using either a 400 µm nozzle for standard prints or an 800 µm nozzle for DOE screening. The constructs, designed with CAD software (3D Builder), were printed in parallelepiped geometries with a volume of 0.2 cm^3 (1x1x0.2 cm). After bioprinting, the constructs were consolidated with solutions containing $CaCl_2$ (Sigma Aldrich) and transglutaminase (Activa WM, Ajinomoto), with some also including 10 U/mL thrombin (Merck T4648 10kU). The solutions, prepared in demineralized water or DMEM (0.026% $CaCl_2$), were sterilized via filtration. Consolidation was carried out at 37°C, 21°C, or 4°C for 15 or 60 minutes, followed by rinsing the structures twice with sterile 0.9% NaCl solution. The detailed panel of consolidation solution prepared is presented in **Supplementary 1**.

2.3 Monitoring of cell viability and Proliferation

Cell viability within the bioprinted 3D constructs was monitored using Calcein green staining. The constructs were incubated at 37°C for 30 minutes with 2 µM Calcein AM (Thermo Fisher Scientific, C1430) and then observed under a fluorescence microscope (Nikon Eclipse Ts2R). Proliferation trends were tracked by cell counting after construct dissociation every 2 to 3 days (n=3). The dissociation protocol, optimized in **Supplementary 1 and Supplementary 2**, involved a two-step process: first, incubating the construct in 3% w/v Collagenase A (Merck, 10103586001) at 37°C for 15-20 minutes, followed by centrifugation at 300g for 5 minutes to separate cells and hydrogel debris. The remaining hydrogel was dissolved in a 0.5 mg/mL alginate lyase (Sigma, A1603) solution, prepared in 100 mM Sodium Citrate buffer (pH 7; Sigma ref 71497), and incubated at 37°C for 3-10 minutes. After another centrifugation at 300g for 5 minutes, the complete cell pellet was recovered, resuspended in 1 mL DMEM (+), and counted using a hemocytometer with Trypan Blue staining. Cell growth rates were calculated based on the total and viable cell counts. The Integral Viable Cell Concentration (IVCC) and Integral Viable Cell number (IVC) were determined using the trapezoidal rule, calculating the area under the curve of cell concentration (cells/mL) and total cell number (cells) as functions of time (days). These metrics were used to describe the global µ or maximal growth rate μ_{max} throughout the culture period. Detailed calculations are presented in **Supplementary 3**.

2.4 Monitoring of cell central carbon metabolism

The lactic acid concentration was quantified on spent media using the L-Lactic Acid Assay from Megazyme (K-LATE, Megazyme) for auto-analyzer procedures. The assay was performed according to the manufacturer's instructions. Each sample was deposited in triplicate in the 96-well plate, and the final absorbance was measured at 340 nm (TECAN infinite®). The glucose concentration was measured by NMR analysis (Bruker Avance III spectrometer - 500MHz 1H resonance frequency). Sample pretreatments necessitate lyophilization and resuspension in Deuterium Oxide (D215F; Eurisotop). An internal reference, the 3-(Trimethylsilyl)propionic-2,2,3,3-d4 acid sodium salt (TMSP) at a concentration of 1,285 g/L, was used for quantification. To further characterize cell metabolism, the average cell-specific rates of lactate production or glucose consumption, respectively q_{lact} and q_{gluc}, and the glucose-to-lactate conversion yield ($Y_{lact/gluc}$) were calculated. Detailed calculations are presented in **Supplementary 3** and list of associated symbols in **Table 1**.

2.5 Characterization of hydrogel properties and 3D cellular structures

For histological staining, samples were rinsed in PBS and fixed in paraformaldehyde (Antigenfix, DiaPath) at 4°C overnight. After PBS rinsing, they were dehydrated through an ethanol gradient (30% to 70%) and stored in 70% ethanol at 4°C. For paraffin embedding, samples were processed in 90% ethanol at 35°C, then in 100% ethanol and Methylcyclohexane at 55°C, before impregnation with paraffin at 60°C. Sections (5 µm thick) were prepared for staining. For Hematoxylin-Eosin (HE) or DAPI staining, sections were deparaffinized, rehydrated, and stained using standard protocols. The HE-stained sections were processed with Hematoxylin and Eosin Fast Quick kit (Diapath 010263), while DAPI (Invitrogen, D3571) staining used a 0.3 µM solution incubated for 15 minutes in the dark, followed by PBS rinsing and mounting in Fluoromount™ (Sigma Aldrich, F4680). For hydrogel ultrastructure characterization, bioprinted constructs were fixed with 2% glutaraldehyde (Electron Microscopy Sciences EMS) in PBS at 4°C for 15 minutes, followed by storage in 2% glutaraldehyde with 0.1 M sodium cacodylate (pH 7.4). Samples were post-fixed with osmium tetroxide, dehydrated in ethanol, and embedded in Epon resin. Ultrathin sections (100 nm) were stained with uranyl acetate and lead citrate and analyzed via Transmission Electron Microscopy (TEM) (Jeol 1400JEM microscope and Orius 1000 camera and Digital Micrograph). TEM images were processed with ImageJ to evaluate microporosity. Hydrogel mechanical characterization to assess elasticity was performed by Dynamic Mechanical Analysis (DMA). DMA measurements were performed according to a protocol already described in a previous work (Chastagnier et al., 2023).

2.6 Image analyses

Images of calcein-stained constructs, DAPI-stained histological sections, and TEM images were processed in Image J software. The images were converted to 8-bit binary, and thresholds were set on the pixel intensity to measure microporosity (TEM) and cell coverage (calcein/DAPI). To measure the per cent of void (porosity), the threshold on the pixels intensity corresponding to the TEM image's light area in the images was set at a value of 140-150 (see **Supplementary 4**). Cell surface coverage in percent was achieved thanks to manual thresholding on DAPI or calcein images (ranges of 24-32 for calcein and 40-70 for DAPI images). Porosity and cell proliferation data were used to compare hydrogel structures and evaluate cell distribution.

2.7 Design of Experiment (DOE) for Bioprinting Optimisation

A Design of Experiment (DOE) approach was used to investigate the impact of bioink formulation, reticulation, and micro-extrusion settings on cell growth and metabolism. The experimental matrix was designed using MODDE13® software (Sartorius) with a fractional factorial plan (**Supplementary 5)**. Proliferation, metabolism, and hydrogel properties data were analysed using Partial Least Squares regression to develop predictive models and optimise bioprinting conditions.

3 RESULTS

We aim to investigate the growth and physiological behaviour of production cell lines in 3D environments compared to traditional 2D cultures. The chosen 3D environment consists of a biocompatible and proliferative biomaterial, structured via 3D bioprinting, which supports cell adherence and growth within a defined volume. The hydrogel used is a proprietary bioink formulation containing 2% w/v Fibrinogen, 2% w/v Alginate, and 5% w/v Gelatin (Marquette et al., 2016; Pourchet et al., 2019). Small-scale bioprinted structures (10×10×2 mm) were seeded with 1.0 x 10^6 cells/mL of hydrogel. After biofabrication, the constructs were consolidated for 1 hour at 37°C in a solution of 3% w/v $CaCl_2$, 4% w/v transglutaminase, and 10 U/mL thrombin. The constructs were cultured in a serum-containing medium for 20 days, with the medium refreshed three times per week. The cell lines selected originate from either kidney (HEK293, MDCK, Vero) or ovary tissues (CHO) of different mammalian species, and have undergone clone selection and spontaneous or induced genetic mutations to be optimised for bioproduction applications.

3.1 3D distribution and organisation of production cell lines

Cell morphology and organisation in 3D cultures were studied to assess cell physiology. Cell lines derived from kidney (HEK293, MDCK, Vero) or ovary tissues (CHO) were evaluated over 20 days. Live cell staining confirmed the survival and proliferation of all lines within the 3D hydrogel structures (**Supplementary 6**). Thanks to this live cell staining, which was complemented by histological analysis (Hematoxylin-Eosin), their 3D organization was also observed.

3.1.1 CHO

During the first 10 days, CHO cells in 3D bioprinted structures remained in single cells or small aggregates. After this period, cells began forming layers on the surface of the hydrogel, which was confirmed by histological staining. Large, irregular cell aggregates (~100 µm in diameter) visible on HE staining formed after 20 days

(Figure 1_a.1) and the DAPI staining revealed a uniform distribution of CHO cells within the hydrogel (see Figure 1_d.1) The ability of CHO cells to secrete matrix metalloproteinases (MMPs) likely facilitated their spread within the hydrogel [32]. It is known that CHO cells originate from a fibroblastic cell in the ovary of a Chinese hamster (Wurm, 2013). While their exact nature is uncertain, the CHO cell organization in 3D resembles the interstitial tissue of the ovary (Alchalabi et al., 2016).

3.1.2 HEK

HEK cells formed spherical/ovoid aggregates in the first 15 days, later spreading as monolayers on the construct's surface. HEK cells growing at the surface presented irregular shapes and formed multilayers as observed in 2D HEK cell cultures. HE histological staining revealed dense, circular cell clusters (~100 µm) after 20 days (Figure 1_a.2). HEK cells, known to secrete MMPs (Liu and Wu, 2006), showed similar colonisation of the hydrogel as CHO cells, but with more regular structures. DAPI staining revealed HEK cells predominantly located at the periphery of the hydrogel, with fewer cells in the deeper layers (Figure 1_d.2). Cell density was 2-fold higher within the hydrogel periphery up to 1.75 mm depth than in its center, which indicates a growth limitation. HEK clusters resemble kidney glomeruli (Ernst and Ruchelli, 2019) or adrenal medulla, and potentially reflect the oncogenic traits of HEK cells (Stepanenko and Dmitrenko, 2015a). HEK cells exact origin remains debated. Studies have shown that they exhibit diverse genetic and phenotypic traits, including epithelial and mesenchymal characteristics (Inada et al., 2016), fibroblast-like markers (Stepanenko and Dmitrenko, 2015b), neuronal lineage genes (Shaw et al., 2002), cancer stem cell features (Debeb et al., 2010), and adrenal gland markers (Lin et al., 2014). Notably, HEK cells grown in 3D aggregates display increased expression of kidney progenitor cell markers, particularly from the glomeruli and proximal tubule (Stepanenko and Dmitrenko, 2015b; Su et al., 2013).

3.1.3 MDCK

MDCK cells initially grew as small aggregates but later organised into monolayers, forming cyst-like structures with a central lumen after 10 days (Figure 1_a.3). This cyst formation, typical of early kidney tubule morphogenesis (Bryant and Mostov, 2008; Zegers et al., 2003), was confirmed by the presence of GP135, an apical membrane marker (Figure 1_c.3) confirming the correct polarisation of the cysts. The renal tubule's origin of MDCK cells is well established [45], and such structures have already been reported for MDCK grown in type-I Collagen and Matrigel 3D hydrogels (Bryant et al., 2014). The DAPI-stained MDCK nuclei showed a 4-fold increase in cell density within the first 1.75 mm depth of the construct compared to the centre, indicating a

proliferation gradient (Figure 1 d.3). MDCK cells can degrade ECM by MMPs secretion (Jordà et al., 2005) which may facilitate their proliferation in the hydrogel by degrading the gelatin.

3.1.4 VERO

Vero cells initially organized as single cells until 10 days of culture but later formed cell layers on the surface of the constructs. Few cells survived inside the hydrogel; a finding consistent with their epithelial origin (Figure 1_a.4 & d.4). The Vero cell line is derived from the kidney of an African Green monkey and is recognised for its epithelial nature. Such behavior was already reported for Vero cells seeded over Collagen or Gelatin scaffolds where they formed monolayers with elongated morphology (Koban et al., 2020a; Nocera et al., 2018; To and Bhunia, 2019). Histological analysis revealed Collagen IV secretion, indicating the recovery of Vero cell epithelial phenotype. Unlike the other cell lines, Vero cells do not secrete MMPs (Liu et al., 2000), which explain their limited ability to colonise the hydrogel.

3.2 Study of cellular kinetics in 3D bioprinted environment

To better understand the physiological changes in 3D bioprinted cultures, we evaluated cell growth and metabolism compared to 2D culture and literature (Figure 3 and Table 2). Growth rates were monitored using an optimised hydrogel dissociation protocol, allowing recovery of ~85% of seeded cells. Growth profiles and central carbon metabolism were studied to estimate each cell type's maximum specific growth and metabolic rates in 3D constructs (Figure 2 & 3). Unlike 2D cultures, where exponential growth began by day 2, all 3D cultures showed a prolonged lag phase of at least 6 days followed by linear growth, without growth arrest after 20 days. Regarding proliferation rate, the specific growth rate (μ) in 3D cultures was reduced by 2 to 9-fold compared to 2D conditions (Figure 3). Comparing metabolic rates, all cell lines demonstrated a shift in specific glucose consumption and lactate production in 3D. In bioprinted 3D cultures, two key metabolic phases (Phase I and Phase II) were identified for all the cell types (Figure 2.B - background colours) where their cell-specific lactate production and glucose consumption rates are constant. Notably, the glucose-to-lactate conversion yield ($Y_{lact/gluc}$) was 2-3 times higher in 2D cultures, indicating metabolic differences between 2D and 3D environments (Table 2). The total lactate production and glucose consumption correlated to the cell growth rate.

3.2.1 CHO cells

A growth phase was identified in CHO cell cultures, starting after a 17-day lag phase. The lag phase was characterised by a growth rate close to zero and cell density maintained under 1.0×10^6 cell/mL of hydrogel. Later,

during the linear growth phase, μ was 0.29 day^{-1}, and the highest cell density reached 2.7 x 10^6 cells/mL of hydrogel. The growth rate during this proliferative phase decreased more than 3-fold compared to the growth rate measured in 2D cultures and the reference growth rate reported for such cells in the literature (Chevalot et al., 1994) (Figure 3 & Table 2). In bioprinted CHO cultures, two key metabolic phases (Phase I and Phase II) were identified based on lactate production and glucose consumption rates. The shift from Phase I to Phase II occurred after 10 days of culture. In Phase I, which coincides with the lag phase, specific lactate production was 1.6 times higher, and glucose consumption increased 10-fold compared to 2D cultures (Figure 2.A & B). In Phase II, correlating with the end of the lag phase and the onset of growth, glucose consumption stabilized, but lactate production doubled compared to Phase I, reaching a rate 4 times higher than in 2D conditions and literature (Ahn and Antoniewicz, 2011). Throughout both phases, CHO cultures exhibited a glucose-to-lactate conversion yield ($Y_{lact/gluc}$) below 1, indicating primarily oxidative metabolism. However, this ratio may be underestimated due to the inability to assess lactate consumption.

3.2.2 HEK

HEK 3D cultures showed linear growth after 15 days of culture. During the lag phase, cell density remained ~0.3 x 10^6 cells/mL of hydrogel. The linear growth phase, starting on day 15, had a growth rate at least twice as slow as in 2D cultures and compared to literature-reported rates for HEK cells (Yang et al., 2019) (see Figure 3 & Table 2). The lag phase ended with a brief rise in cell density to 0.7 x 10^6 cells/mL between days 8 and 13, followed by a drop back to 0.3 x 10^6 cells/mL before growth resumed on day 15. The main growth phase lasted 5 days, with the highest density reaching 5.0 x 10^6 cells/mL of hydrogel.

HEK bioprinted cultures also exhibited two key metabolic phases, like CHO cells. The transition from Phase I to Phase II coincided with the onset of the main growth phase. In Phase I, specific glucose consumption and lactate production rates increased 20-fold and 9-fold, respectively, compared to 2D cultures. Both rates decreased 5-fold in Phase II but remained higher than in 2D cultures and reported values (Henry et al., 2011). During both metabolic phases, the $Y_{lact/gluc}$ ratio in HEK cultures exceeded 1, suggesting glucose was mainly converted to lactate via fermentation or that additional carbon sources contributed to lactate accumulation. The $Y_{lact/gluc}$ ratio in 2D cultures was even higher, exceeding the aerobic glycolysis threshold, indicating the involvement of other carbon sources, such as amino acids, in pyruvate and lactate production (Petiot et al., 2015).

3.2.3 MDCK

MDCK cells exhibited a 6-day lag phase, followed by a linear growth phase (Figure 2.B). During the lag phase, cell density stayed below 0.3 x 10^6 cells/mL of hydrogel. The growth phase reached a maximum rate of 0.10 day^{-1}, with a peak cell density of ~2.0 x 10^6 cells/mL of bioink. This growth rate represents a 9-fold reduction compared to 2D cultures and reported values for adherent MDCK cells (Bock et al., 2009). Metabolic analysis revealed two phases aligning with the lag and growth phases. In Phase I, specific glucose consumption increased 20-fold, and lactate production increased 8-fold compared to 2D cultures. Both rates halved in Phase II but remained higher than those observed in 2D cultures and the literature (Bock et al., 2009). Like HEK cells, MDCK cells exhibited a lactate-to-glucose ratio ($Y_{lact/gluc}$) greater than 1, indicating a predominantly fermentative metabolism.

3.2.4 VERO

Unlike other cell lines, Vero cells in a 3D environment exhibited slow, continuous proliferation from day 1, with a growth rate of 0.08 day^{-1}—5 to 15 times lower than in 2D cultures and reported values (Petiot et al., 2010). Vero cells reached a maximum density of 3.5 x 10^6 cells/mL of hydrogel. Despite only showing one proliferative phase, Vero cells displayed two distinct metabolic phases, with a shift occurring after 6 days. Notably, Vero cells were the only ones to show equal or reduced metabolic activity in 3D compared to 2D cultures. During Phase I, glucose consumption was nearly zero, and lactate production was reduced 5-fold compared to 2D conditions. The $Y_{lact/gluc}$ ratio was extremely high, indicating lactate production relied primarily on non-glucose carbon sources like amino acids. In Phase II, glucose consumption matched 2D cultures, while lactate production dropped 4-fold compared to standard cultures (Petiot et al., 2010) and the cells shifted to a more oxidative metabolism ($Y_{lact/gluc} < 1$).

3.2.5 Impact of 3D seeding density on cell proliferation and organisation

Like 2D or suspension cultures, low seeding density in 3D bioprinting can result in reduced growth rates, extended lag phases, and low cell densities (Rodriguez et al., 2001). The micro-extrusion process in bioprinting significantly affects post-printing cell recovery (Chastagnier et al., 2023; Lemarié et al., 2021). In our study, post-printing cell recovery rates were evaluated, showing significant losses of 65-80% for HEK, MDCK, and CHO cells, while Vero cells showed much better recovery with only 20% loss. Seeding densities were tripled to address this, and cell growth was monitored over 20 days. This increase in seeding density reduced or eliminated the lag phase in all cases (**Supplementary 7**). Maximal cell densities were significantly boosted, with a 2-fold increase for Vero and MDCK cells and a 5-fold increase for CHO cells, which reached a maximum density of 10 x 10^6 cells/mL of

hydrogel. Despite these improvements, the maximal densities remained much lower than those typically achieved in standard fed-batch processes, where CHO cells can reach up to 25 x 10^6 cells/mL without specific process intensification (Ruhl et al., 2020). HEK cells showed a more irregular growth pattern, with a brief increase in density followed by stabilisation at around 1-1.5 x 10^6 cells/mL of hydrogel.

Increasing the initial cell density reduced the lag phase but did not eliminate it or significantly impact the growth rates. Importantly, the cell's morphology, organisation and distributions were like those described with lower starting cell density, with reduced cell concentration in the center of the construct for HEK and MDCK cells (data not shown). In conclusion, while increasing the seeding density accelerated the onset of 3D cell growth, it did not notably enhance growth rates in any bioprinted culture (Figure 3). The observed cell gradient in constructs seeded with HEK or MDCK cells suggests that nutrient and oxygen diffusion within the hydrogel may have a stronger impact on cell proliferation kinetics and distribution.

3.3 Impact of Hydrogel Properties on 3D Cell Proliferation and Spreading

The previous results indicated limited cell proliferation and poor survival in the centre of 3D hydrogels, suggesting that the properties of the hydrogel itself were a key factor limiting cell growth and distribution. In 3D cultures, cell behavior is influenced by various factors, including cell-cell and cell-matrix interactions, mechanical properties, microporosity, and the diffusion of essential molecules (Baker and Chen, 2012; Colom et al., 2014). These factors help recreate a more physiological environment but can also restrict cell proliferation. Furthermore, several process parameters in bioprinting can affect biomaterial properties and post-printing cell recovery.

In this part of the study, we aimed to identify biofabrication parameters affecting cell proliferation and spreading within the hydrogel. We used HEK cells, which had the longest lag phase (10 days), as a model to study the impact of biofabrication parameters on hydrogel properties. Cultures were carried out for 10 days, using a high initial seeding concentration of 3.0 x 10^6 cells/mL of hydrogel. Eight biofabrication parameters were screened in a design of experiments (DOE) (**Supplementary 5**), including bioink formulation, filament diameter, and hydrogel consolidation factors (temperature, duration, and concentrations of transglutaminase, $CaCl_2$, thrombin, and DMEM). Data from 178 samples across 26 conditions were analysed using Partial Least Square (PLS) regression

to model the relationship between hydrogel properties and cell proliferation (see Table 3 for R^2, Q^2, and reproducibility). Only the regression coefficient $R^2 > 0.5$ models were considered acceptable.

Mechanical properties of the hydrogel were assessed using Young's modulus, and microporosity was evaluated via transmission electron microscopy (TEM) and dynamic mechanical analysis (DMA). Immediately after printing, Young's modulus ranged from 0.31 ± 0.24 kPa in less elastic hydrogels to 29.5 ± 7.1 kPa in the most elastic ones. After 10 days of culture, these values increased to 8.5 ± 2.1 kPa and 60.7 ± 12.0 kPa, respectively. It should be noted that a few hydrogel samples were too smooth and fragile to be measured (<0.01 kPa). Temperature, transglutaminase, $CaCl_2$ concentration, and consolidation duration had the most significant impact in PLS models on hydrogel elasticity (Figure 4_b.1), with elasticity increasing by 2-log depending on these factors. Hydrogel microporosity was inversely correlated with elasticity ($R^2 = -0.67$), with porosities ranging from 44 ± 5% to 84 ± 3% on day 1 and from 41 ± 6% to 74 ± 4% on day 10 (Figure 4_a.2). Transglutaminase and $CaCl_2$ concentration, as well as consolidation duration, had the greatest influence on microporosity (Figure 4_b.2), with higher transglutaminase levels resulting in denser hydrogel structures due to increased cross-linking of gelatin (Bertoni et al., 2006) and fibrinogen (Poole et al., 2022). Among them, transglutaminase concentration was the most decisive factor.

We then examined the effect of hydrogel microstructure and mechanical properties on HEK cell growth kinetics. Cell proliferation was measured by both cell counting after hydrogel dissociation and image analysis of live-stained cells. While predictive models for cell density and growth rate had poor fits ($R^2 < 0.5$), significant differences in growth were observed across the DOE conditions. The best-performing condition extended the growth phase up to 10 days, with a growth rate of 0.13 d^{-1}, compared to just 3 days in the initial protocol. This optimal condition also reduced cell mortality after bioprinting to 25%, compared to 67% in the initial setup. A maximum cell density of 10 x 10^6 cells/mL of hydrogel was achieved, 15 times higher than the initial condition. The poor fit is likely due to low reproducibility between samples, with high variability and low precision in the analytical methods used. Dissociation and image analysis had 39% and 60% precision levels, respectively. Image analysis of 3D constructs was particularly variable due to heterogeneous cell distribution, while hydrogel dissolution and counting involved multiple steps that impacted cell recovery. These results were achieved using hydrogel formulation A, printed with a 400 µm nozzle and consolidated for 60 minutes at 21°C in a solution containing 0.4% w/v transglutaminase, 1.4% w/v $CaCl_2$, and 10 U/mL thrombin in deionized water. This solution

had physiological osmolality (~300 mOsmol/kg), compared to the initial condition's higher osmolality (~648 mOsmol/kg). Microporosity was positively correlated with both the growth rate ($R^2 = 0.6$) and the volume occupied by live cells ($R^2 = 0.8$) (**Supplementary 8**), suggesting that cell proliferation is strongly influenced by hydrogel microstructure, likely due to improved nutrient and oxygen diffusion or reduced space for cell aggregation. Further studies are needed to fully understand the relationship between diffusion kinetics, microporosity, and cell growth in different hydrogel formulations.

4 DISCUSSION

Although HEK, CHO, MDCK, and Vero cells have been previously cultured in 3D environments (Koban et al., 2020b; Ouyang et al., 2015), detailed descriptions of their proliferation, metabolic kinetics, and organization in 3D have been lacking. Our study sheds new light on these cell lines' distinct 3D growth patterns, with some reverting to native tissue characteristics. For example, MDCK cells formed polarised cysts, while Vero cells created epithelial layers. The 3D hydrogel, which mimics the extracellular matrix (ECM), promoted more in vivo-like behavior than conventional 2D cultures. These results are consistent with prior studies showing that 3D environments closely replicate *in vivo* conditions (Ravi et al., 2015; Souza et al., 2018a), enabling cells to grow, interact with their surroundings, and recreate tissue microstructures (Anton et al., 2015; Souza et al., 2018a). Cells grown in 3D exhibit more in vivo-like functions, including gene expression, growth rates (Lagies et al., 2020; Rybkowska et al., 2023; Souza et al., 2018b), metabolic activity (Ikari et al., 2021). These effects are largely driven by integrin- and cadherin-mediated interactions with the ECM(Hynes, 2002; Klezovitch and Vasioukhin, 2015), which influence cellular signaling, morphology, and proliferation. The 3D matrix environment provided distinct cues to each cell line, resulting in varied organizational patterns despite shared tissue origins (e.g., HEK, MDCK, Vero). These differences may stem from the cells' derivation from different tissues or species and the effects of decades of genetic modifications and clonal selection in bioproduction cell lines.

Cell localization varied by cell lines ; HEK and MDCK cells concentrated at the hydrogel periphery due to nutrient limitations, while CHO cells displayed a uniform distribution, likely due to their metabolic flexibility, including adaptation to carbon source deprivation with a lactate consumption switch (Martínez et al., 2013). DAPI staining of histological sections further confirmed cell regionalization, with HEK and MDCK cells preferring the outer 1.75 mm of the construct, consistent with the literature on limited proliferation in 3D due to oxygen and nutrient diffusion challenges already observed in 3D matrix (Lesher-Pérez et al., 2017).

The ability of CHO, HEK and MDCK cells to secrete matrix metalloproteinases (MMPs), enabling ECM degradation and cell migration, likely contributed to the differences in cell behavior. MMP secretion, especially collagenases (MMP-1, MMP-8 and MMP-13) and gelatinases (MMP-2 and MMP-9), enables cells to degrade ECM components like collagen and gelatin, facilitating processes essential for migration, wound healing, angiogenesis, or tumor invasion (Kandhwal et al., 2022).

In standard 2D cultures, production cell lines typically exhibit high proliferation rates, with doubling times of 12-24 hours, which is ideal for intensifying bioproduction processes (Cervera et al., 2011). However, in our study, cell lines grown in 3D environments exhibited significantly slower proliferation, reduced growth rates, and lower maximum cell densities. This slower growth in 3D is well-documented and is thought to better mimic *in vivo* conditions (Lagies et al., 2020; Rybkowska et al., 2023; Souza et al., 2018b). In 3D cultures, proliferation inhibition is often due to increased cell-cell and cell-matrix interactions, which trigger multiple signalling pathways that regulate cell growth, apoptosis, and differentiation (Anton et al., 2015). The cell densities achieved in 3D cultures (2.0 to 5.0 x 10^6 cells/mL of hydrogel) were much lower than those in 2D cultures, where values range from 7.0 x 10^6 to 25.0 x 10^6 cells/mL in non-intensified processes (Liu et al., 2009; Ruhl et al., 2020). In typical 2D and suspension cultures, fast-growing cell lines exhibit metabolic deregulation, often leading to aerobic glycolysis, characterized by rapid glucose consumption, lactate accumulation, and reduced oxidative respiration also reported as "Warburg effect"

Our findings highlight notable metabolic changes in 3D-cultured cell lines. CHO, HEK, and MDCK cells exhibited higher metabolic activity than in 2D cultures, while Vero cells showed minimal changes, likely because they grew mostly on the surface, resembling 2D growth. The increase in global metabolic activity in 3D cultures, as seen in other studies [80], suggests a closer alignment with *in vivo* conditions. Specifically, the lactate-to-glucose ratio was reduced by at least half during growth in 3D, indicating less reliance on lactic fermentation and a shift toward increased mitochondrial respiration, consistent with other 3D models (Rybkowska et al., 2023). Diffusion gradients may drive this enhanced metabolic efficiency in 3D environments within the hydrogel, which regulate nutrient availability and balance metabolic pathways. While our study provides insight into the metabolic changes in 3D cultures, further analysis is required to fully understand these mechanisms across different cell lines.

The effect of the 3D environment and biofabrication tools on cell behavior was assessed using a fractional factorial design (DOE), identifying key parameters influencing both hydrogel properties and cell proliferation. Hydrogel

consolidation had the greatest impact on the mechanical and microstructural properties of the 3D environment. Adjusting transglutaminase activity—by modifying concentration, treatment duration, or temperature—led to forming denser networks with distinct microarchitectures and mechanical characteristics. The microstructure of the biofabricated support plays a critical role in promoting or limiting cell proliferation. The ability of cells to access nutrients and oxygen and remove metabolic waste largely depends on the thickness of the 3D construct, as well as the composition and structure of the matrix. These factors directly influence molecular diffusion rates, crucial for maintaining cell health and function (Lesher-Pérez et al., 2017). For example, nutrient diffusion is limited to about 300 µm in static liver tissue cultures and normal tissues. illustrating how matrix design can significantly impact cell behavior in 3D environments.

5 CONCLUSION

This study provides key insights into the physiological changes and factors influencing cell behavior in 3D cell cultures. We demonstrated that even highly mutated, non-primary cell lines can regain in vivo-like characteristics when grown in 3D biofabricated environments. These cell lines proliferated within 3D structures, with growth regulated by biofabrication protocols and hydrogel microporosity. We observed increased metabolic activity and reduced fermentative behavior in these 3D constructs. Beyond medical applications like regenerative medicine and drug testing, 3D bioprinting holds potential for bioproduction by supporting dense cell colonization and enhancing metabolic efficiency. This highlights the broad utility of 3D bioprinted cell cultures for both therapeutic and industrial purposes.

6 ACKNOWLEDGEMENTS

The Sartorius company funded this work. We sincerely thank the people from Sartorius who were invested and contributed to the project, Magali Barbaroux, Julia Niemann, David Pollard and Oscar Reif. We also acknowledge the Centre Commun de RMN (CCRMN) from Université Lyon 1, for the NMR acquisitions and the CIQLE from Université Lyon 1 for the transmission electron microscopy imaging.

7 DATA AVAILABILITY

The raw/processed data required to reproduce these findings cannot be shared at this time due to legal or ethical reasons.

8 LEGENDS

FIGURE 1: Evaluation of cell distribution and organization in 3D bioprinted constructs. Histological studies of bioprinted constructs at day 20: (A) Hematoxylin-Eosin staining, dark arrows indicate (a.2) cell aggregates, (a.3) cysts or, (a.4) cell layers, (B) Collagen IV staining (brown) indicated with dark arrows, (C) Staining of polarized MDCK GP135 membrane protein (red) indicated with white arrows, and cell nuclei with DAPI (blue), and (D) Cell distribution on full construct slice observed by nuclei staining with DAPI (blue), the numbers indicate the % of surface colonized by cells according to image analyses (d.2 & d.3) the orange dot line indicate the proliferation limit..

FIGURE 2: Proliferation and Metabolic profiles for 3D bioprinted cell line. Growth curve (dark blue line) and **specific rate of glucose consumption** (orange bar) and **lactate production** (grey bar) of HEK, MDCK, CHO and Vero in 2D (A) and in 3D bioprinted constructs seeded with 1.0 x 10^6 cell/mL of bioink (n= 2 or 3) (B). The red arrows indicate the start of growth phase, and the blue arrows indicate de peak of maximal cell density. In (B) the two metabolic phases are identified by two different background colors. (C) presents a comparison of growth rates in 2D (dark blue) and 3D constructs seeded with 1.0 x 10^6 cell/mL of bioink (yellow) or 3.0 x 10^6 cell/mL of bioink (red) (n= 2 or 3).

FIGURE 3: Growth rate in 3D bioprinted cell line. Comparison of growth rates axtracted from the literature (grey) or measured in 2D (dark blue) and 3D constructs seeded with 1.0 x 10^6 cell/mL of bioink (yellow) or 3.0 x 10^6 cell/mL of bioink (red) (n= 2 or 3).

FIGURE 4: Biofabrication impact on HEK cell proliferation in 3D environment. (a.1 & a.2) Distribution of hydrogel mechanical properties of the 26 tested conditions (day 1 & 10 : n>2),(a.3 & a.4) microporosity of the hydrogel (day 1 & 10: n>3), (a.5) cell density achieved at Day 10 and (a.6) associated growth rates (n=2). Associated impact of biofabrication factor's (b.1_DMA measures ; b.2_ Microporosity).

TABLE 1: List of symbols

TABLE 2: Comparison of growth and metabolic parameters in 2D cultures and 3D bioprinted constructs seeded with 1.0 x10^6 cell/mL of bioink. The several parameters are presented: Growth rate, specific metabolic rates of glucose consumption and lactate production, and average lactate to glucose molar ratio.

TABLE 3: PLS models quality assessment. Regression coefficients (R^2, Q^2) and reproducibility of the predictive models established with DOE experiment. The quality of predictive PLS model fitting was evaluated on three variables. First, the regression coefficient R2 represents the variation of the response explained by the model. The second indicator Q2, is the predictive ability of the model, also known as model predictive power. It represents the ability to generalize to new, unseen data. According to the recommendation of MODDE13® software user guide, a Q2 tends to underestimate the model, it should be over 0.1 to have a significant model and a Q2 over 0.5 with (R2 - Q2) < 0.3 indicates a good model. The last indicator is reproducibility, representing the response variation in replicates of the same condition compared to the total response variation. This parameter is expected to be superior to 0.5.

SUPPLEMENTARY 1: Characterization of cross-linking and dissociation solutions (pH and osmolality).

SUPPLEMENTARY 2: Dissociation protocols screening efficiency. Dissociation protocols efficiency was evaluated in terms of cell viability, percent of cell recovery and estimated % of hydrogel dissociation.

SUPPLEMENTARY 3: Methods used to calculate Cell growth rates, Integral Viable Cell Concentration (IVCC) and Integral Viable Cell number (IVC).

SUPPLEMENTARY 4: Procedure for hydrogel micro-porosity quantification. Example of image Analysis on TEM images. A.1 and B.1 show the TEM imaging of two different hydrogels microstructures. Figures A.2 and B.2 show the setting of threshold for measurement of the percent of void surface (in green).

SUPPLEMENTARY 5: DOE factorial fractional design, associated parameters selected (Bioink formulation, Nozzle diameter, crosslinking conditions) **and the associated quantified response in growth rate** when available.

SUPPLEMENTARY 6: Growth trend monitored by calcein staining of 3D printed hydrogels over 20-days for HEK293, MDCK, Vero and CHO cells. Bioprinted structures were seeded at 1.0 x10^6 cell/mL.

SUPPLEMENTARY 7: Compared growth profile for seeded cell lines at 1 and 3 x 10^6 cell/ml of bioink.

SUPPLEMENTARY 8: Correlation matrix extracted from the DOE experiment, showing the correlation between factors and responses. Form. : Formulation of the bioink ; Diam Ø : diameter of the printing nozzle; TAG

: Transglutaminase concentration; Thr. : Thrombine concentration; Calcein : fluorescent surface of the bioprinted ; Xmax : Cell concentration ; µ specific growth rate between D1 and D10; Micro. : Microporosité calculated on TEM images.

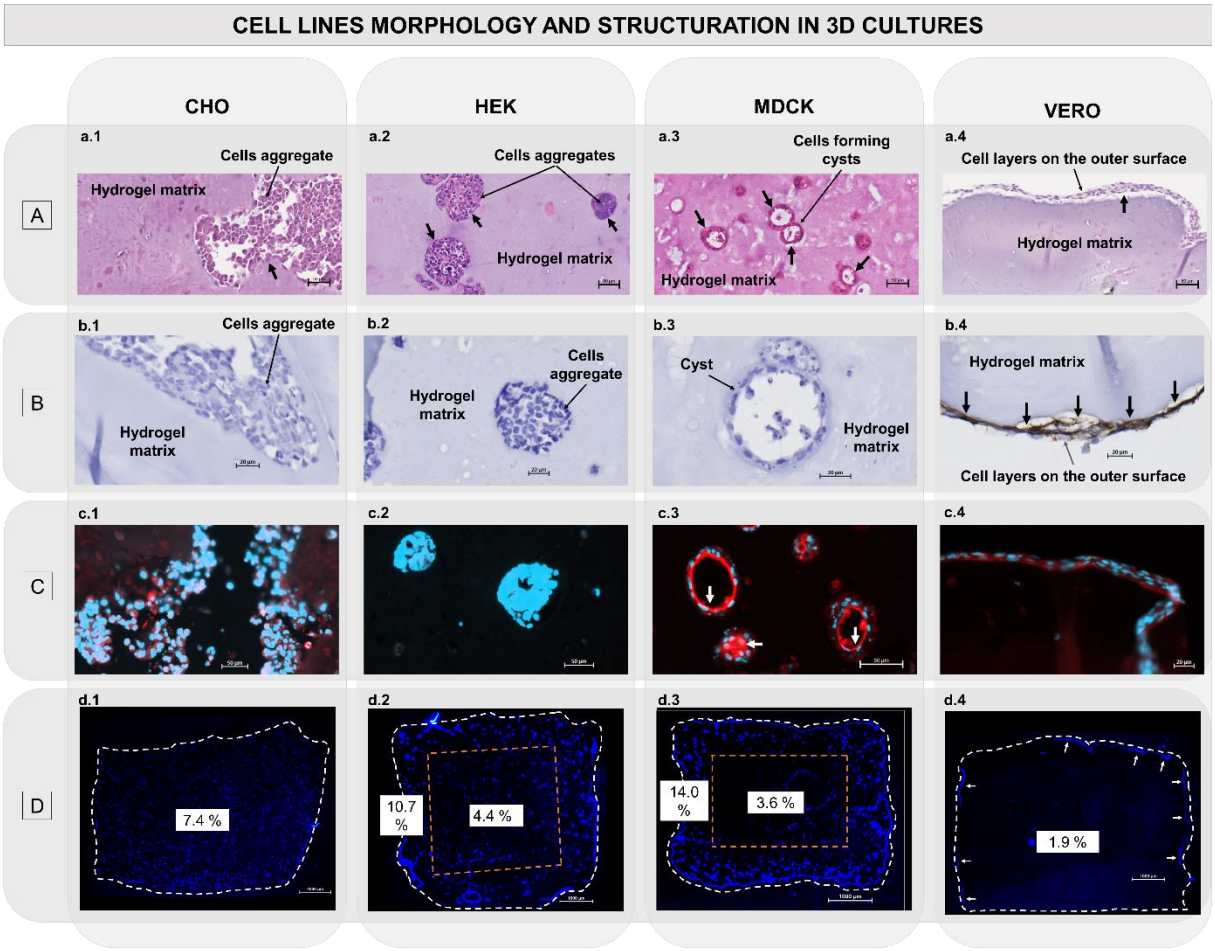

FIGURE 1: Evaluation of cell distribution and organization in 3D bioprinted constructs. Histological studies of bioprinted constructs at day 20: (A) Hematoxylin-Eosin staining, dark arrows indicate (a.2) cell aggregates, (a.3) cysts or, (a.4) cell layers, (B) Collagen IV staining (brown) indicated with dark arrows, (C) Staining of polarized MDCK GP135 membrane protein (red) indicated with white arrows, and cell nuclei with DAPI (blue), and (D) Cell distribution on full construct slice observed by nuclei staining with DAPI (blue), the numbers indicate the % of surface colonized by cells according to image analyses (d.2 & d.3) the orange dot line indicate the proliferation limit.

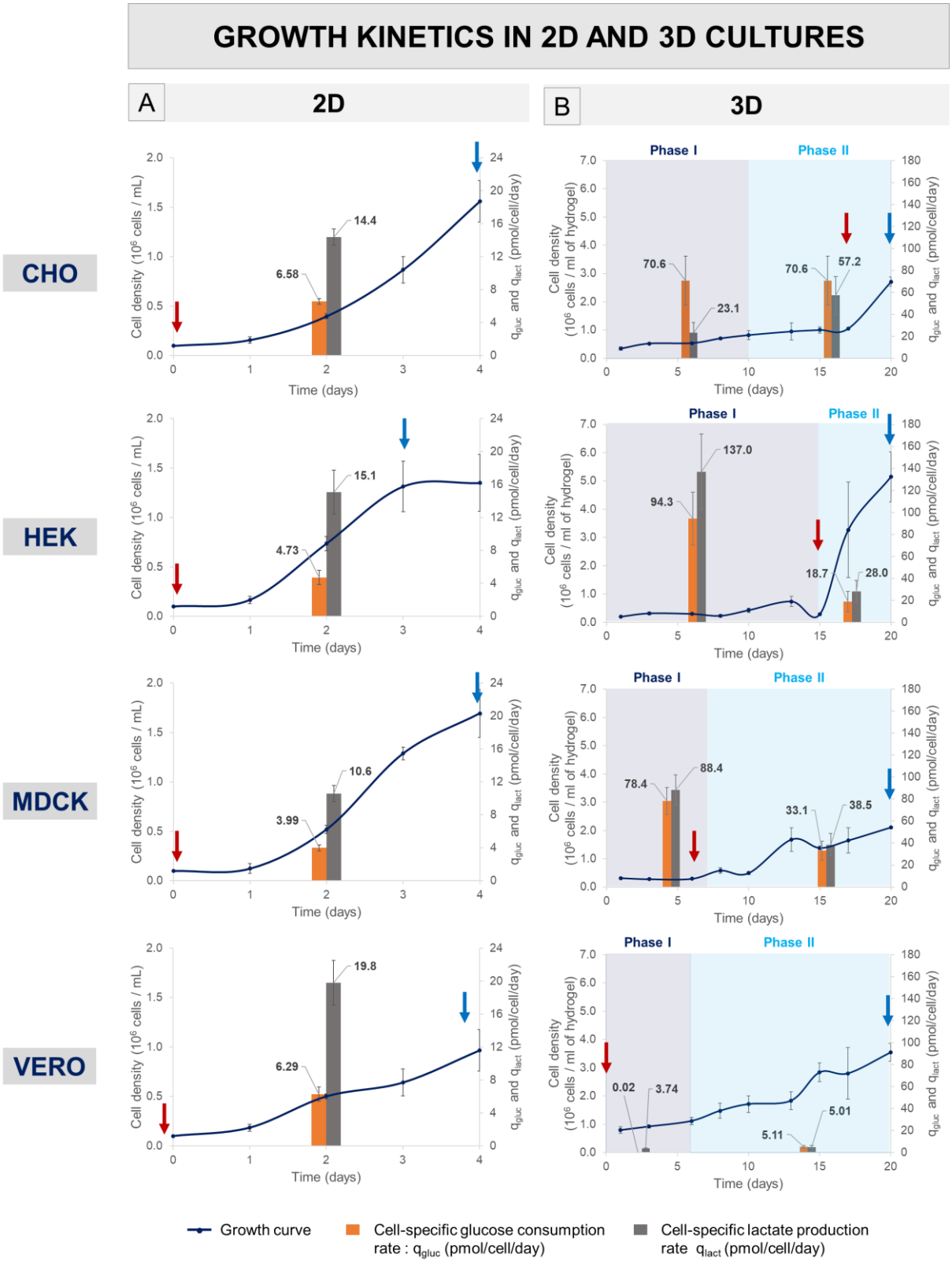

FIGURE 2: Proliferation and Metabolic profiles for 3D bioprinted cell line. Growth curve (dark blue line) and **specific rate of glucose consumption** (orange bar) and **lactate production** (grey bar) of HEK, MDCK, CHO and Vero in 2D (A) and in 3D bioprinted constructs seeded with 1.0 x 10^6 cell/mL of bioink (n= 2 or 3) (B). The red arrows indicate the start of growth phase, and the blue arrows indicate de peak of maximal cell density. In (B) the two metabolic phases are identified by two different background colors. (C) presents a comparison of growth rates in 2D (dark blue) and 3D constructs seeded with 1.0 x 10^6 cell/mL of bioink (yellow) or 3.0 x 10^6 cell/mL of bioink (red) (n= 2 or 3).

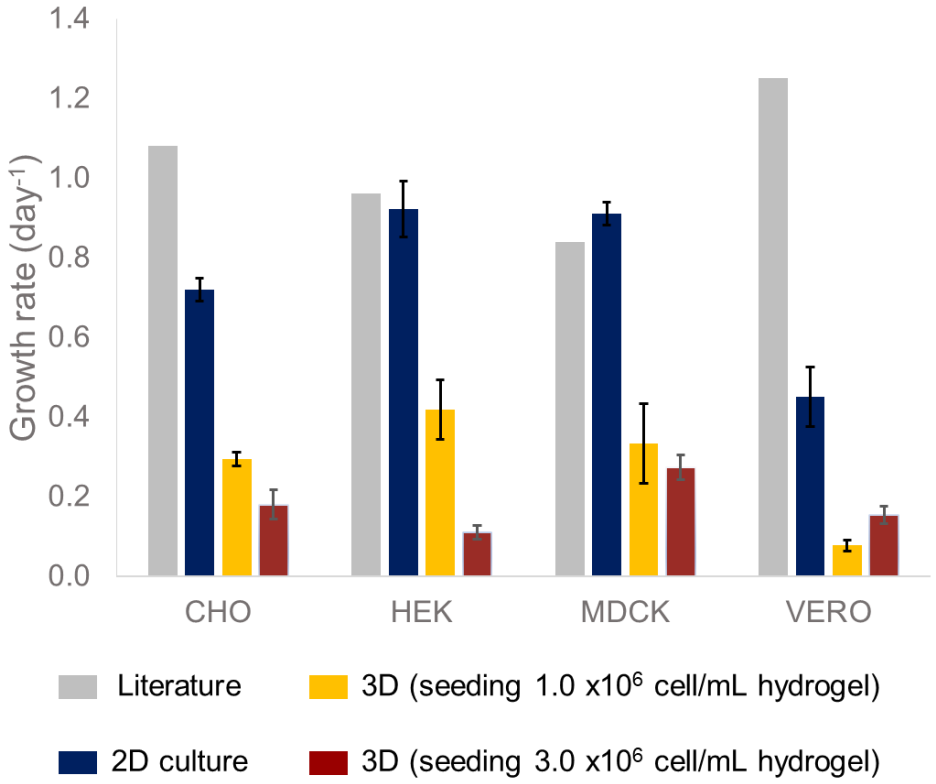

FIGURE 3: Growth rate in 3D bioprinted cell line. Comparison of growth rates extracted from the literature (grey) or measured in 2D (dark blue) and 3D constructs seeded with 1.0 x 10^6 cell/mL of bioink (yellow) or 3.0 x 10^6 cell/mL of bioink (red) (n= 2 or 3).

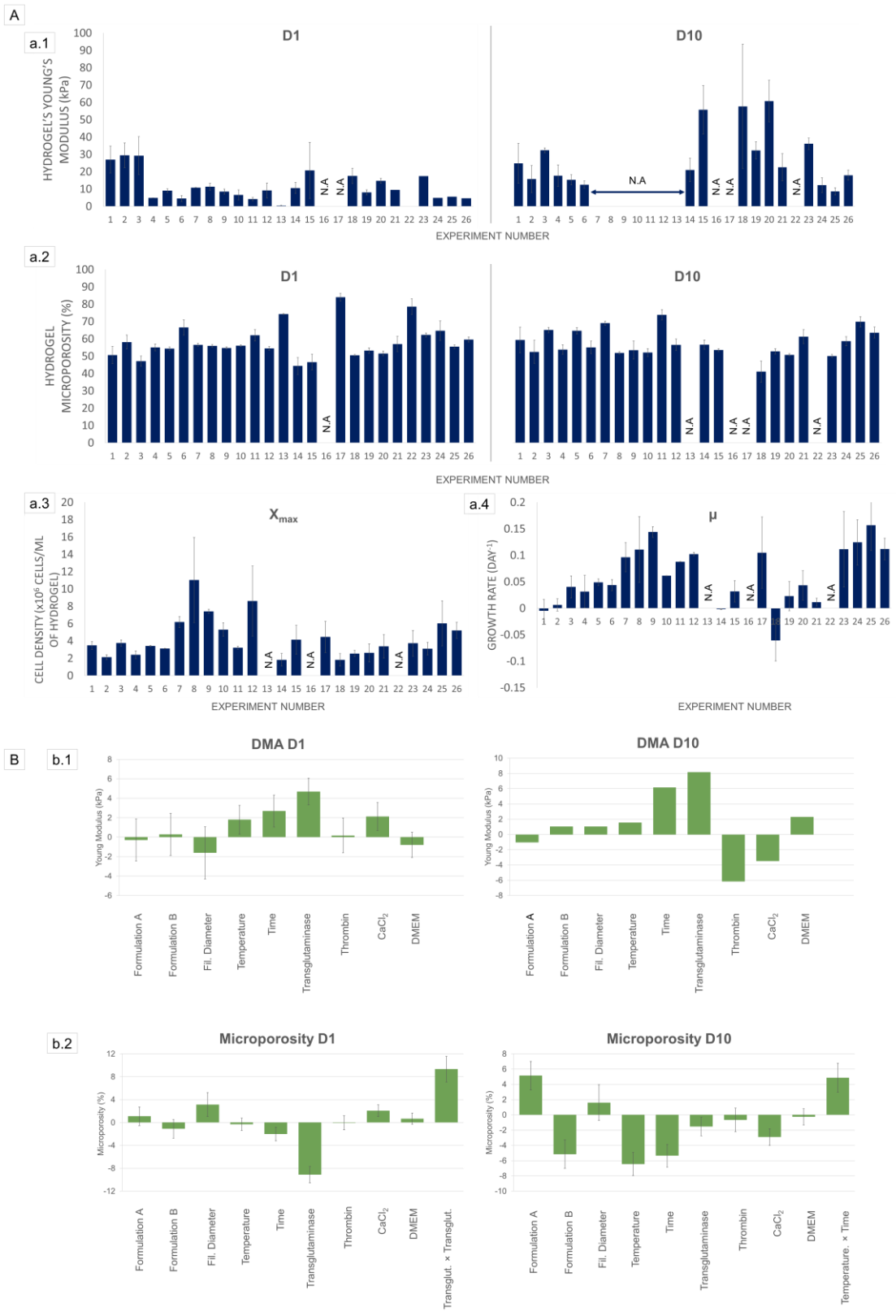

FIGURE 4: Biofabrication impact on HEK cell proliferation in 3D environment. (a.1 & a.2) Distribution of hydrogel mechanical properties of the 26 tested conditions (day 1 & 10 : n>2),(a.3 & a.4) microporosity of the hydrogel (day 1 & 10: n>3), (a.5) cell density achieved at Day 10 and (a.6) associated growth rates (n=2). Associated impact of biofabrication factor's (b.1_DMA measures ; b.2_ Microporosity).

Symbols	
Δ	Variation of parameter (delta)
δ	Statistical error on a parameter
IVCC	Integral Viable Cells Concentration
IVC	Integral Viable Cells number (in one bioprinted construct)
t	Time (days)
t_0	Starting time of the studied period (days).
n	Number of points on the curve / number of studied points
X	Cell concentration per mL of hydrogel in 3D cultures or per mL of supernatant in 2D cultures (cell/mL) at time t.
X_0	Cell concentration (cell/mL) at time t_0
X_{av}	Average cell concentration during Δt (cell/mL)
x	Total cell number (cells) in one bioprinted construct
μ	Growth rate (day^{-1})
μ_{max}	Maximal growth rate (exponential growth)
M	Concentration of the studied metabolite (lactate or glucose) at a time t
M_0	Concentration of the studied metabolite (lactate or glucose) at a time t_0
q_{lact}	Cell-specific lactate production rate
q_{gluc}	Cell-specific glucose consumption rate
q_M	Cell-specific production rate of the studied metabolite
$Y_{lact/gluc}$	Glucose to lactate conversion yield (mol/mol)

TABLE 1: List of symbols

		2D	3D - Phase I	3D - Phase II	Reference	Source
CHO	μ (d^{-1})	0.72 ± 0.03	0.29 ± 0.02		0.96	(Chevalot et al., 1994)
	q_{gluc} (pmol/cell/day)	6.58 ±0.91	70.6 ±22.13		4.82	(Ahn and Antoniewicz, 2011)
	q_{lact} (pmol/cell/day)	14.4 ±1.95	23.1 ±9.27	57.2 ±17.26	7.19	
	$Y_{lact/gluc}$	2.19	0.33	0.81	NA	NA
HEK	μ (d^{-1})	0.92 ± 0.07	0.42 ± 0.07		0.84	(Yang et al., 2019)
	q_{gluc} (pmol/cell/day)	4.73 ±0.85	94.3 ±24.22	18.7 ±9.24	3.34	(Henry et al., 2011)
	q_{lact} (pmol/cell/day)	15.1 ±2.66	137 ±34.24	28 ±10.13	5.04	
	$Y_{lact/gluc}$	3.19	1.45	1.50	NA	NA
MDCK	μ (d^{-1})	0.91 ± 0.03	0.33 ± 0.06		1.08	(Bock et al., 2009)
	q_{gluc} (pmol/cell/day)	3.99 ±0.36	78.4 ±12.19	33.1 ±8.72	3.72	
	q_{lact} (pmol/cell/day)	10.6 ±0.98	88.4 ±13.60	38.5 ±10.08	3.38	
	$Y_{lact/gluc}$	2.66	1.13	1.16	NA	NA
VERO	μ (d^{-1})	0.45 ± 0.08	0.08 ± 0.01		0.46 to 1.25	(Arifin et al., 2010; Petiot et al., 2010)
	q_{gluc} (pmol/cell/day)	6.29 ±0.85	0.02 ± 0.00	5.11 ±1.19	8.40 to 11.52	
	q_{lact} (pmol/cell/day)	19.8 ±2.70	3.74 ±0.48	5.01 ±1.17	9.12 to 18.24	
	$Y_{lact/gluc}$	3.15	187.00	0.98	NA	NA

TABLE 2: Comparison of growth and metabolic parameters in 2D cultures and 3D bioprinted constructs seeded with 1.0 x10^6 cell/mL of bioink. Several parameters are presented: Growth rate, specific metabolic rates of glucose consumption and lactate production, and average lactate to glucose molar ratio.

		R^2	Q^2	Reproducibility
Hydrogel microstructure	**DMA day 0 (kPa)**	0.61	0.51	0.66
	DMA day 10 (kPa)	0.70	0.55	0.84
	Microporosity day 1	0.70	0.62	0.88
	Microporosity day 10	0.52	0.45	0.56
Cell proliferation	**Xmax day 10 (cell/g)**	0.30	0.03	0.29
	Xmax day 10 (total cell)	0.41	0.05	0.68
	μ_{max} (d^{-1})	0.17	0.07	0.41
	Calcein day 10 (%)	0.10	-0.09	0.32

TABLE 3: PLS models quality assessment. Regression coefficients (R^2, Q^2) and reproducibility of the predictive models established with DOE experiment.

9 LITERATURE

Agarwal S, Saha S, Balla VK, Pal A, Barui A, Bodhak S. 2020. Current Developments in 3D Bioprinting for Tissue and Organ Regeneration–A Review. *Front Mech Eng* **6**.

Ahn WS, Antoniewicz MR. 2011. Metabolic flux analysis of CHO cells at growth and non-growth phases using isotopic tracers and mass spectrometry. *Metab Eng* **13**:598–609. http://dx.doi.org/10.1016/j.ymben.2011.07.002.

Alchalabi ASH, Rahim H, Aklilu E, Al-Sultan II, Aziz AR, Malek MF, Ronald SH, Khan MA. 2016. Histopathological changes associated with oxidative stress induced by electromagnetic waves in rats' ovarian and uterine tissues. *Asian Pacific Journal of Reproduction* **5**:301–310. http://dx.doi.org/10.1016/j.apjr.2016.06.008.

Anton D, Burckel H, Josset E, Noel G. 2015. Three-dimensional cell culture: A breakthrough in vivo. *Int J Mol Sci* **16**:5517–5527.

Arifin MA, Mel M, Abdul Karim MI, Ideris A. 2010. Production of newcastle disease virus by vero cells grown on cytodex 1 microcarriers in a 2-litre stirred tank bioreactor. *J Biomed Biotechnol* **2010**.

Baker BM, Chen CS. 2012. Deconstructing the third dimension-how 3D culture microenvironments alter cellular cues. *J Cell Sci* **125**:3015–3024.

Bastin G, Chotteau V, Vande Wouwer A. 2021. Metabolic flux analysis of VERO cells under various culture conditions. *Processes* **9**:1–20.

Bertoni F, Barbani N, Giusti P, Ciardelli G. 2006. Transglutaminase reactivity with gelatine: Perspective applications in tissue engineering. *Biotechnol Lett* **28**:697–702.

Bock A, Sann H, Schulze-Horsel J, Genzel Y, Reichl U, Möhler L. 2009. Growth behavior of number distributed adherent MDCK cells for optimization in microcarrier cultures. *Biotechnol Prog* **25**:1717–1731.

Bryant DM, Mostov KE. 2008. From cells to organs: Building polarized tissue. *Nat Rev Mol Cell Biol* **9**:887–901.

Bryant DM, Roignot J, Datta A, Overeem AW, Kim M, Yu W, Peng X, Eastburn DJ, Ewald AJ, Werb Z, Mostov KE. 2014. A molecular switch for the orientation of epithelial cell polarization. *Dev Cell* **31**:171–187. http://dx.doi.org/10.1016/j.devcel.2014.08.027.

Cervera L, Gutiérrez S, Gòdia F, Segura MM. 2011. Optimization of HEK 293 cell growth by addition of non-animal derived components using design of experiments. *BMC Proc* **5**:P126. http://www.biomedcentral.com/1753-6561/5/S8/P126.

Chagnon-Lessard S, Jean-Ruel H, Godin M, Pelling AE. 2021. Mechanotransduction of Strain Regulates an Invasive Phenotype in Newly Transformed Epithelial Cells. *Front Phys* **9**:1–11.

Chastagnier L, el-Kholti N, Essayan L, Thomann C, Courtial EJ, Marquette CA, Petiot E. 2023. Deciphering dermal fibroblast behavior in 3D bioprinted dermis constructs. *Bioprinting* **32**:e00275.

Chevalot I, Visvikis A, Nabet P, Engasser JM, Marc A. 1994. Production of a membrane-bound proteins, the human gamma-glutamyl transferase, by CHO cells cultivated on microcarriers, in aggregates and in suspension. *Cytotechnology* **16**:121–129.

Colom A, Galgoczy R, Almendros I, Xaubet A, Farré R, Alcaraz J. 2014. Oxygen diffusion and consumption in extracellular matrix gels: Implications for designing three-dimensional cultures. *J Biomed Mater Res A* **102**:2776–2784.

Debeb BG, Zhang X, Krishnamurthy S, Gao H, Cohen E, Li L, Rodriguez AA, Landis MD, Lucci A, Ueno NT, Robertson F, Xu W, Lacerda L, Buchholz TA, Cristofanilli M, Reuben JM, Lewis MT, Woodward WA. 2010. Characterizing cancer cells with cancer stem cell-like features in 293T human embryonic kidney cells. *Mol Cancer* **9**:1–12.

Ernst LM, Ruchelli ED. 2019. Color Atlas of Human Fetal and Neonatal Histology Second Edition 157 p.

Guo J, Wang Y, Sachs F, Meng F. 2014. Actin stress in cell reprogramming. *Proc Natl Acad Sci U S A* **111**:E5252–E5261.

Henry O, Jolicoeur M, Kamen A. 2011. Unraveling the metabolism of HEK-293 cells using lactate isotopomer analysis. *Bioprocess Biosyst Eng* **34**:263–273.

Hutchinson L, Kirk R. 2011. High drug attrition rates - Where are we going wrong? *Nat Rev Clin Oncol* **8**:189–190.

Hynes RO. 2002. Integrins: Bidirectional, Allosteric Signaling Machines. *Cell Press* **110**:673–687.

Ikari R, Mukaisho KI, Kageyama S, Nagasawa M, Kubota S, Nakayama T, Murakami S, Taniura N, Tanaka H, Kushima R, Kawauchi A. 2021. Differences in the central energy metabolism of cancer cells between conventional 2d and novel 3d culture systems. *Int J Mol Sci* **22**:1–13.

Inada M, Izawa G, Kobayashi W, Ozawa M. 2016. 293 Cells Express Both Epithelial As Well As Mesenchymal Cell Adhesion Molecules. *Int J Mol Med* **37**:1521–1527.

Jordà M, Olmeda D, Vinyals A, Valero E, Cubillo E, Llorens A, Cano A, Fabra À. 2005. Upregulation of MMP-9 in MDCK epithelial cell line in response to expression of the Snail transcription factor. *J Cell Sci* **118**:3371–3385.

Kandhwal M, Behl T, Singh S, Sharma N, Arora S, Bhatia S, Al-Harrasi A, Sachdeva M, Bungau S. 2022. Role of matrix metalloproteinase in wound healing. *Am J Transl Res* **14**:4391–4405. www.ajtr.org.

Kawaue T, Yow I, Pan Y, Le AP, Lou Y, Loberas M, Shagirov M, Teng X, Prost J, Hiraiwa T, Ladoux B, Toyama Y. 2023. Inhomogeneous mechanotransduction defines the spatial pattern of apoptosis-induced compensatory proliferation. *Dev Cell* **58**:267-277.e5.

Klezovitch O, Vasioukhin V. 2015. Cadherin signaling: Keeping cells in touch. *F1000Res* **4**.

Koban R, Lam T, Schwarz F, Kloke L, Bürge S, Ellerbrok H, Neumann M. 2020a. Simplified bioprinting-based 3d cell culture infection models for virus detection. *Viruses* **12**.

Koban R, Lam T, Schwarz F, Kloke L, Bürge S, Ellerbrok H, Neumann M. 2020b. Simplified Bioprinting-Based 3D Cell Culture Infection Models for Virus Detection. *Viruses* **12**.

Kuystermans D, Al-Rubeai M. 2015. Biopharmaceutical Products from Animal Cell Culture 717–757 p.

Lagies S, Schlimpert M, Neumann S, Wäldin A, Kammerer B, Borner C, Peintner L. 2020. Cells grown in three-dimensional spheroids mirror in vivo metabolic response of epithelial cells. *Commun Biol* **3**. http://dx.doi.org/10.1038/s42003-020-0973-6.

Lemarié L, Anandan A, Petiot E, Marquette C, Courtial E-J. 2021. Rheology, simulation and data analysis toward bioprinting cell viability awareness. *Bioprinting* **21**.

Lesher-Pérez SC, Kim GA, Kuo CH, Leung BM, Mong S, Kojima T, Moraes C, Thouless MD, Luker GD, Takayama S. 2017. Dispersible oxygen microsensors map oxygen gradients in three-dimensional cell cultures. *Biomater Sci* **5**:2106. https://pmc.ncbi.nlm.nih.gov/articles/PMC5678941/.

Lin YC, Boone M, Meuris L, Lemmens I, Van Roy N, Soete A, Reumers J, Moisse M, Plaisance S, Drmanac R, Chen J, Speleman F, Lambrechts D, Van De Peer Y, Tavernier J, Callewaert N. 2014. Genome dynamics of the human embryonic kidney 293 lineage in response to cell biology manipulations. *Nat Commun* **5**.

Liu CH, Wu PS. 2006. Characterization of matrix metalloproteinase expressed by human embryonic kidney cells. *Biotechnol Lett* **28**:1725–1730.

Liu H, Liu XM, Li SC, Wu BC, Ye LL, Wang QW, Chen ZL. 2009. A high-yield and scaleable adenovirus vector production process based on high density perfusion culture of HEK 293 cells as suspended aggregates. *J Biosci Bioeng* **107**:524–529. http://dx.doi.org/10.1016/j.jbiosc.2009.01.004.

Liu S, Netzel-Arnett S, Birkedal-Hansen H, Leppla SH. 2000. Tumor cell-selective cytotoxicity of matrix metalloproteinase-activated anthrax toxin. *Cancer Res* **60**:6061–6067.

Marquette CA, Chastagnier L, Da Sousa B, Chocarro-Wrona C, Courtial EJ, Rae E, Thomann C, Carre A, Essayan L, Pasuch AJ, Mosnier A, Devillard C, Petiot E, Lemarié L, Matera EL, Simoes M, Dumontet C, Cuella Martin C, Pechtimaldjian L, Pécheur EI, Maguer-Satta V, Michelet M, Plissonnier ML, Archer F, Moreau K, Dufaud M, Zaupa C, Balloul JM, Pruvost Q, Dauphin T, Mosser M, Pragnère S. 2024. Unlocking the potential of bio-inspired bioinks: A collective breakthrough in mammalian tissue bioprinting. *Bioprinting* **41**:e00351.

Marquette CA, Pourchet L, Thepot A, Dos Santos M. 2016. Method for manufacturing body substitutes by additive deposition. France US11566234B2.

Martinac B, Nikolaev YA, Silvani G, Bavi N, Romanov V, Nakayama Y, Martinac AD, Rohde P, Bavi O, Cox CD. 2020. Cell membrane mechanics and mechanosensory transduction. *Curr Top Membr* 1st ed. Elsevier Inc. Vol. 86 83–141 p. http://dx.doi.org/10.1016/bs.ctm.2020.08.002.

Martínez VS, Dietmair S, Quek LE, Hodson MP, Gray P, Nielsen LK. 2013. Flux balance analysis of CHO cells before and after a metabolic switch from lactate production to consumption. *Biotechnol Bioeng* **110**:660–666.

Martínez-Monge I, Albiol J, Lecina M, Liste-Calleja L, Miret J, Solà C, Cairó JJ. 2019. Metabolic flux balance analysis during lactate and glucose concomitant consumption in HEK293 cell cultures. *Biotechnol Bioeng* **116**:388–404.

Matai I, Kaur G, Seyedsalehi A, McClinton A, Laurencin CT. 2020. Progress in 3D bioprinting technology for tissue/organ regenerative engineering. *Biomaterials* **226**:119536. https://doi.org/10.1016/j.biomaterials.2019.119536.

Mih JD, Marinkovic A, Liu F, Sharif AS, Tschumperlin DJ. 2012. Matrix stiffness reverses the effect of actomyosin tension on cell proliferation. *J Cell Sci* **125**:5974–5983.

Moussa HI, Logan M, Chan WY, Wong K, Rao Z, Aucoin MG, Tsui TY. 2018. Pattern-dependent mammalian cell (Vero) morphology on tantalum/silicon oxide 3D nanocomposites. *Materials* **11**:17–20.

Nocera AD, Comín R, Salvatierra NA, Cid MP. 2018. Development of 3D printed fibrillar collagen scaffold for tissue engineering. *Biomed Microdevices* **20**:1–13.

Ouyang L, Yao R, Chen X, Na J, Sun W. 2015. 3D printing of HEK 293FT cell-laden hydrogel into macroporous constructs with high cell viability and normal biological functions. *Biofabrication* **7**:015010. https://iopscience.iop.org/article/10.1088/1758-5090/7/1/015010.

Petiot E, Cuperlovic-Culf M, Shen CF, Kamen A. 2015. Influence of HEK293 metabolism on the production of viral vectors and vaccine. *Vaccine* **33**:5974–5981.

Petiot E, Guedon E, Blanchard F, Gény C, Pinton H, Marc A. 2010. Kinetic characterization of vero cell metabolism in a serum-free batch culture process. *Biotechnol Bioeng* **107**:143–153.

Poole LG, Kopec AK, Flick MJ, Luyendyk JP. 2022. Cross-linking by tissue transglutaminase-2 alters fibrinogen-directed macrophage proinflammatory activity. *Journal of Thrombosis and Haemostasis* **20**:1182–1192.

Pourchet LJ, Thepot A, Albouy M, Courtial EJ, Boher A, Blum LJ, Marquette CA. 2017. Human Skin 3D Bioprinting Using Scaffold-Free Approach. *Adv Healthc Mater* **6**:1601101. http://doi.wiley.com/10.1002/adhm.201601101.

Pourchet L, Petiot E, Loubière C, Olmos E, Dos Santos M, Thépot A, Loïc BJ, Marquette CA. 2019. Large 3D bioprinted tissue: Heterogeneous perfusion and vascularization. *Bioprinting* **13**:e00039. https://linkinghub.elsevier.com/retrieve/pii/S2405886618300277.

Ravi M, Paramesh V, Kaviya SR, Anuradha E, Paul Solomon FD. 2015. 3D cell culture systems: Advantages and applications. *J Cell Physiol* **230**:16–26.

Reinhart D, Damjanovic L, Kaisermayer C, Sommeregger W, Gili A, Gasselhuber B, Castan A, Mayrhofer P, Grünwald-Gruber C, Kunert R. 2019. Bioprocessing of Recombinant CHO-K1, CHO-DG44, and CHO-S: CHO Expression Hosts Favor Either mAb Production or Biomass Synthesis. *Biotechnol J* **14**:1–11.

Rodriguez EN, Perez M, Casanova P, Martinez L. 2001. Effect of Seed Cell Density on Specific Growth Rate Using CHO Cells as Model. *Animal Cell Technology: From Target to Market* **2**:434–437.

Ruhl S, de Almeida N, Carpio M, Rupprecht J, Greller G, Matuszczyk J-C. 2020. A Rapid, Low-Risk Approach for Process Transfer of Biologics from Development to Manufacturing Scale. *Bioprocess Int* **19**:44–51.

Rybkowska P, Radoszkiewicz K, Kawalec M, Dymkowska D, Zabłocka B, Zabłocki K, Sarnowska A. 2023. The Metabolic Changes between Monolayer (2D) and Three-Dimensional (3D) Culture Conditions in Human Mesenchymal Stem/Stromal Cells Derived from Adipose Tissue. *Cells* **12**.

Schulze M, Niemann J, Wijffels RH, Matuszczyk J, Dirk |, Martens E. 2021. Rapid intensification of an established CHO cell fed-batch process. https://doi.org/10.1002/btpr.3213.

Shaw G, Morse S, Ararat M, Graham FL. 2002. Preferential transformation of human neuronal cells by human adenoviruses and the origin of HEK 293 cells. *The FASEB journal : official publication of the Federation of American Societies for Experimental Biology* **16**:869–871.

Souza AG, Silva IBB, Campos-Fernandez E, Barcelos LS, Souza JB, Marangoni K, Goulart LR, Alonso-Goulart V. 2018a. Comparative Assay of 2D and 3D Cell Culture Models: Proliferation, Gene Expression and Anticancer Drug Response. *Curr Pharm Des* **24**:1689–1694.

Souza AG, Silva IBB, Campos-Fernandez E, Barcelos LS, Souza JB, Marangoni K, Goulart LR, Alonso-Goulart V. 2018b. Comparative Assay of 2D and 3D Cell Culture Models: Proliferation, Gene Expression and Anticancer Drug Response. *Curr Pharm Des* **24**:1689–1694. https://pubmed.ncbi.nlm.nih.gov/29623827/.

Stepanenko AA, Dmitrenko V V. 2015a. HEK293 in cell biology and cancer research: Phenotype, karyotype, tumorigenicity, and stress-induced genome-phenotype evolution. *Gene* **569**:182–190. http://dx.doi.org/10.1016/j.gene.2015.05.065.

Stepanenko AA, Dmitrenko V V. 2015b. HEK293 in cell biology and cancer research: Phenotype, karyotype, tumorigenicity, and stress-induced genome-phenotype evolution. *Gene* **569**:182–190. http://dx.doi.org/10.1016/j.gene.2015.05.065.

Su G, Zhao Y, Wei J, Han J, Chen L, Xiao Z, Chen B, Dai J. 2013. The effect of forced growth of cells into 3D spheres using low attachment surfaces on the acquisition of stemness properties. *Biomaterials* **34**:3215–3222. http://dx.doi.org/10.1016/j.biomaterials.2013.01.044.

To CZ, Bhunia AK. 2019. Three dimensional vero cell-platform for rapid and sensitive screening of Shiga-toxin producing Escherichia coli. *Front Microbiol* **10**:1–15.

Wahl A, Sidorenko Y, Dauner M, Genzel Y, Reichl U. 2008. Metabolic flux model for an anchorage-dependent MDCK cell line: Characteristic growth phases and minimum substrate consumption flux distribution. *Biotechnol Bioeng* **101**:135–152.

Walsh G, Walsh E. 2022. Biopharmaceutical benchmarks 2022. *Nat Biotechnol* **40**:1722–1760.

Wong HL, Wang MX, Cheung PT, Yao KM, Chan BP. 2007. A 3D collagen microsphere culture system for GDNF-secreting HEK293 cells with enhanced protein productivity. *Biomaterials* **28**:5369–5380.

Wurm FM. 2013. CHO quasispecies-Implications for manufacturing processes. *Processes* **1**:296–311.

Yang J, Guertin P, Jia G, Lv Z, Yang H, Ju D. 2019. Large-scale microcarrier culture of HEK293T cells and Vero cells in single-use bioreactors. *AMB Express* **9**. https://doi.org/10.1186/s13568-019-0794-5.

Yuan J, Xu WW, Jiang S, Yu H, Poon HF. 2018. The scattered twelve tribes of HEK293. *Biomedical and Pharmacology Journal* **11**:621–623.

Zamorano F, Wouwer A Vande, Bastin G. 2010. Metabolic flux analysis of CHO-320 cells: Undetermined network and effect of measurement errors. *IFAC Proceedings Volumes (IFAC-PapersOnline)* **43**:437–442.

Zegers MMP, O'Brien LE, Yu W, Datta A, Mostov KE. 2003. Epithelial polarity and tubulogenesis in vitro. *Trends Cell Biol* **13**:169–176.

CELL LINES MORPHOLOGY AND STRUCTURATION IN 3D CULTURES

CHO

HEK

MDCK

VERO

A

a.1

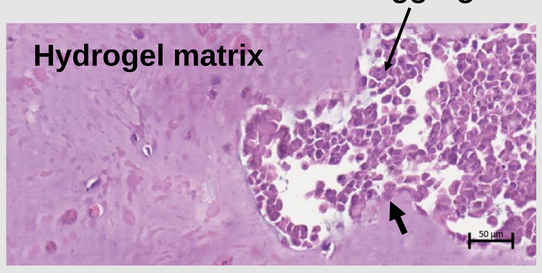

a.2

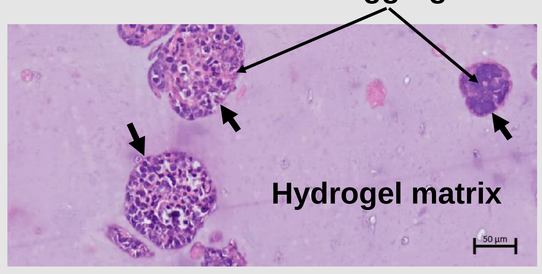

a.3

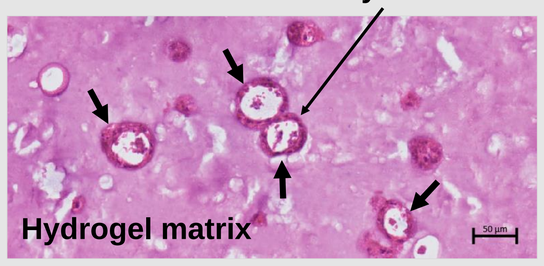

a.4

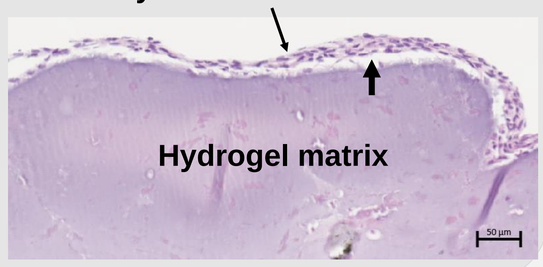

B

b.1

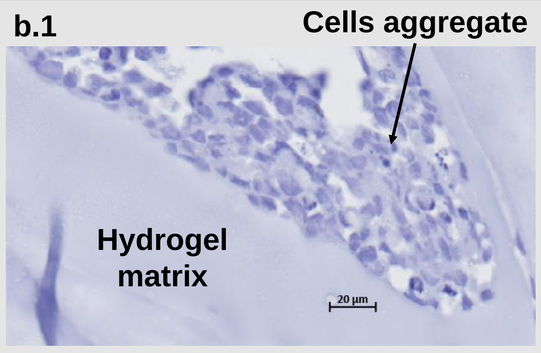

b.2

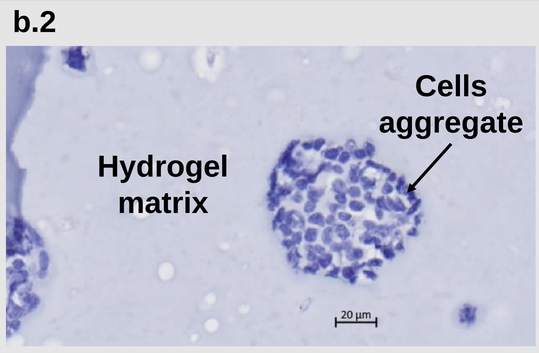

b.3

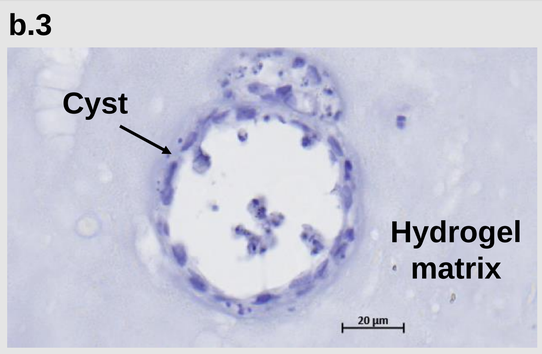

b.4

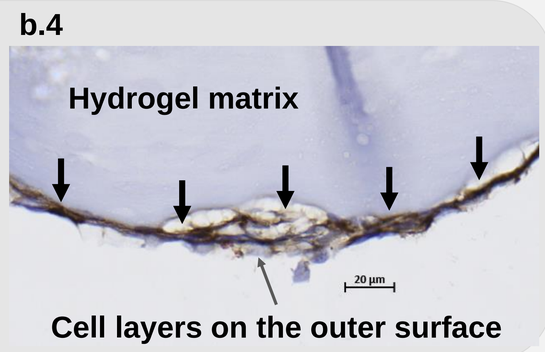

C

c.1

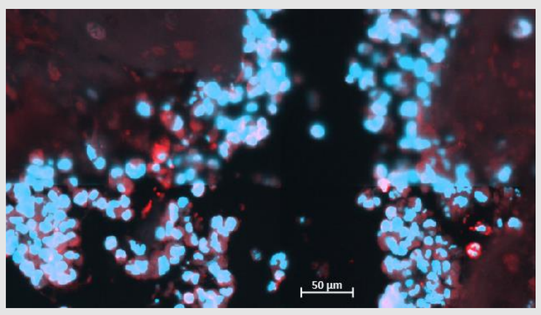

c.2

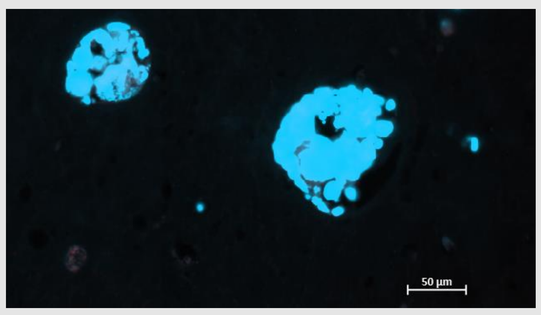

c.3

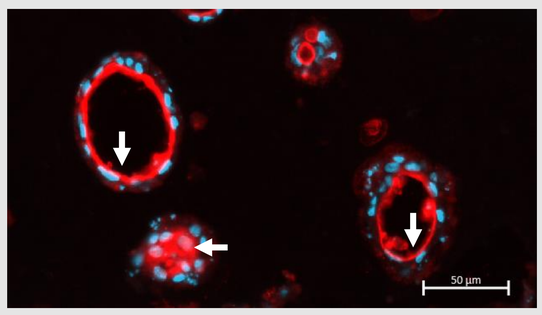

c.4

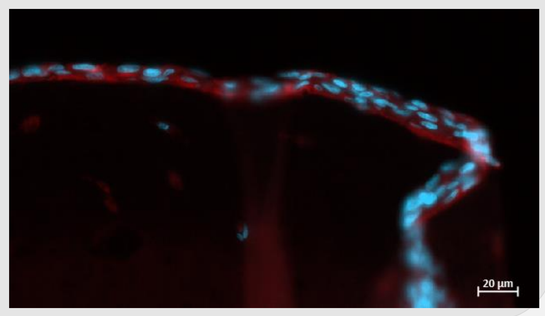

D

d.1

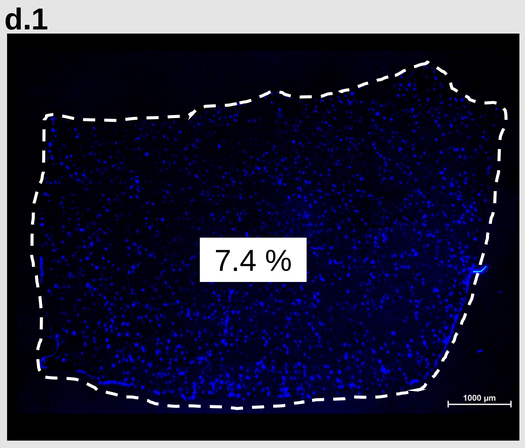

d.2

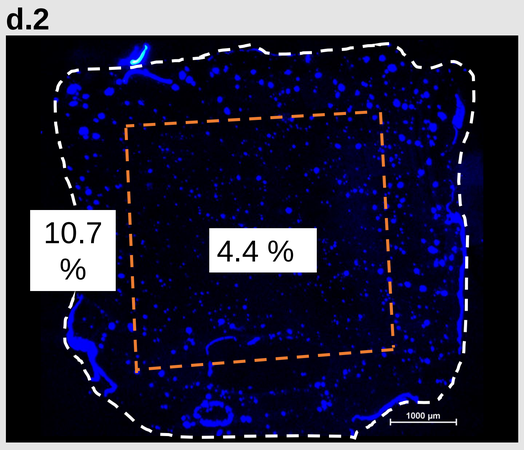

d.3

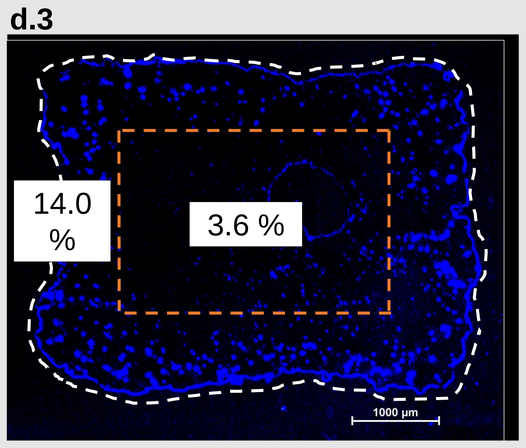

d.4

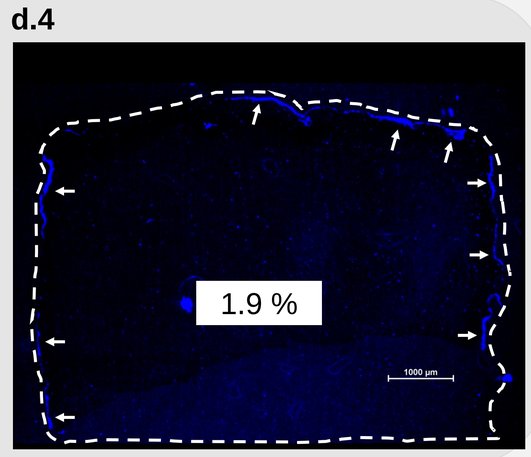

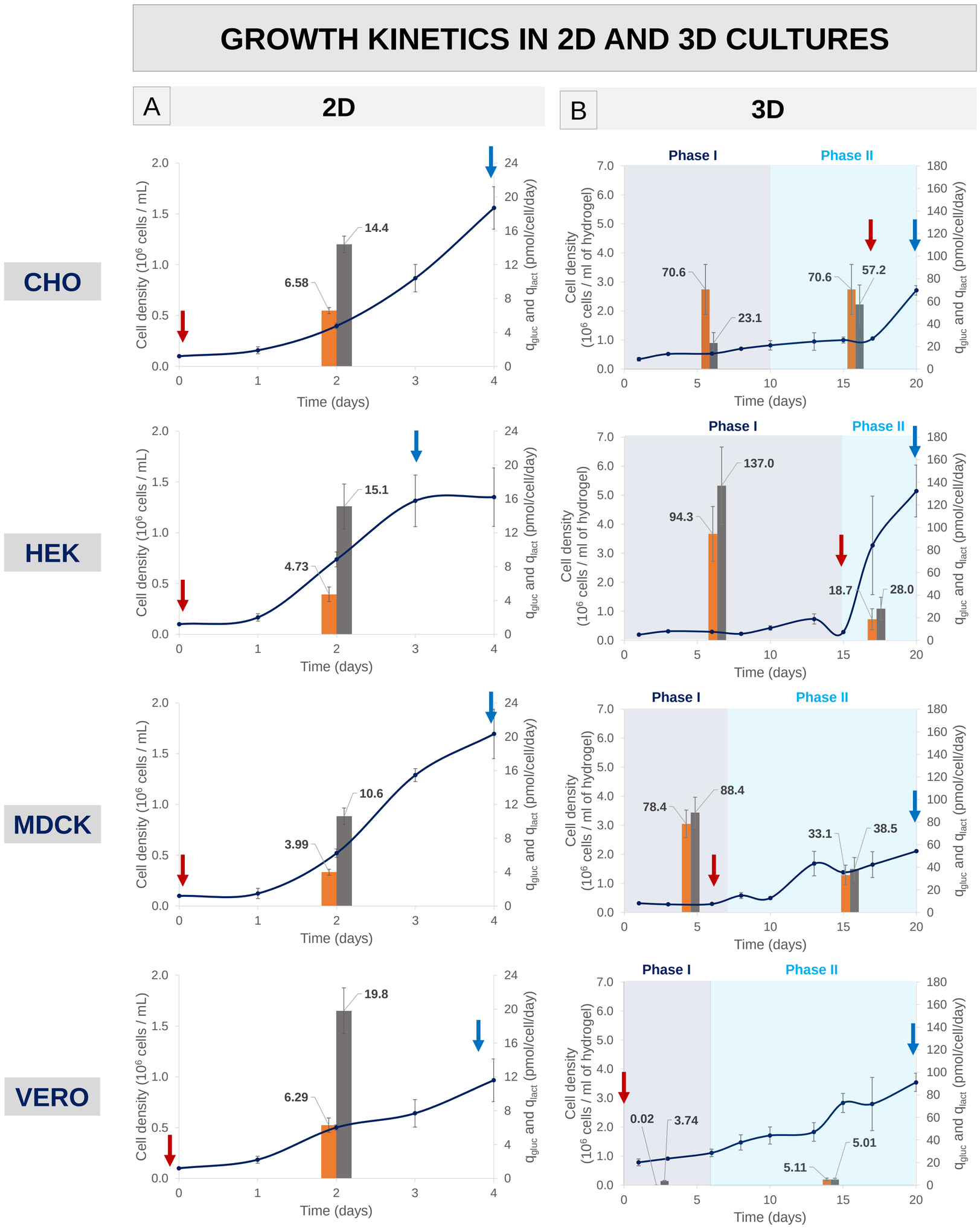

GROWTH KINETICS IN 2D AND 3D CULTURES

A **2D** | B **3D**

CHO

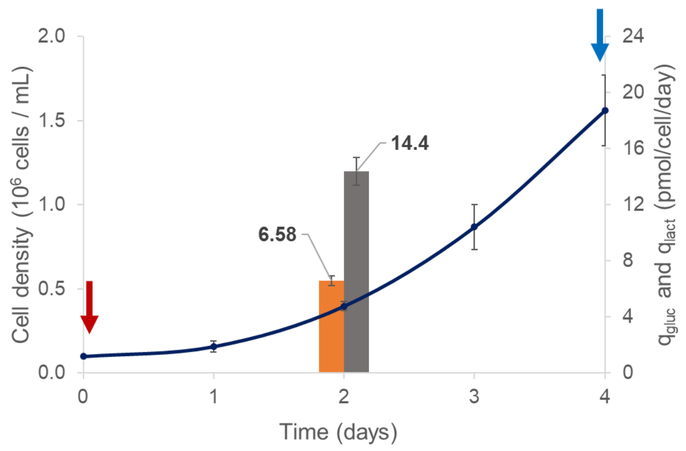

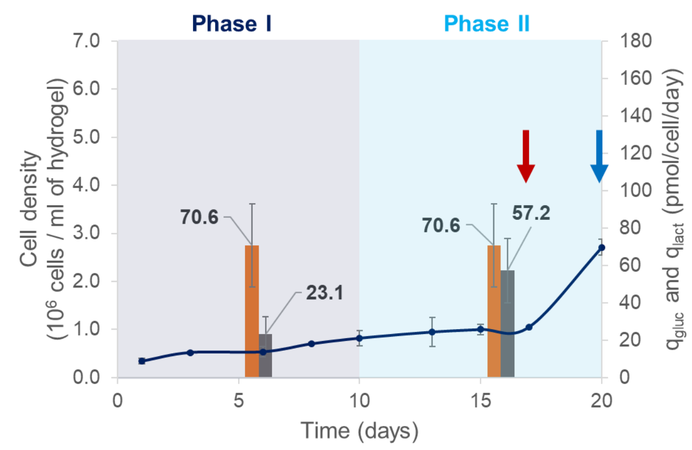

HEK

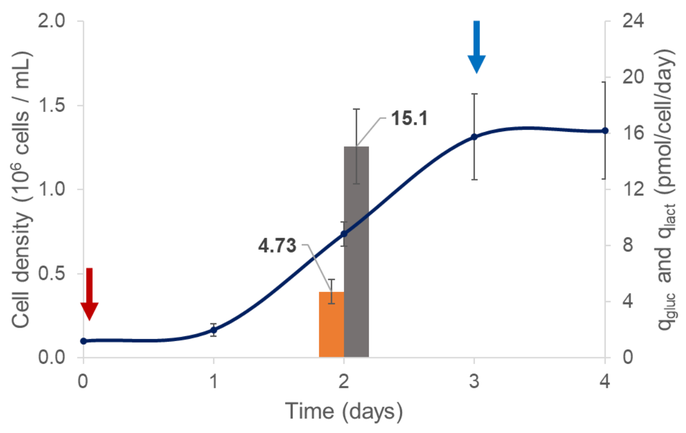

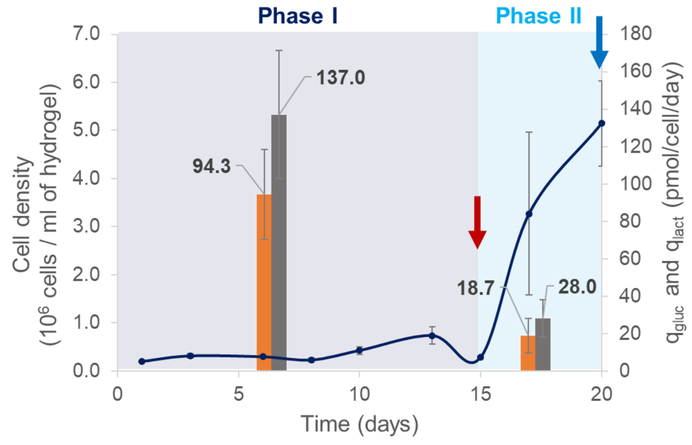

MDCK

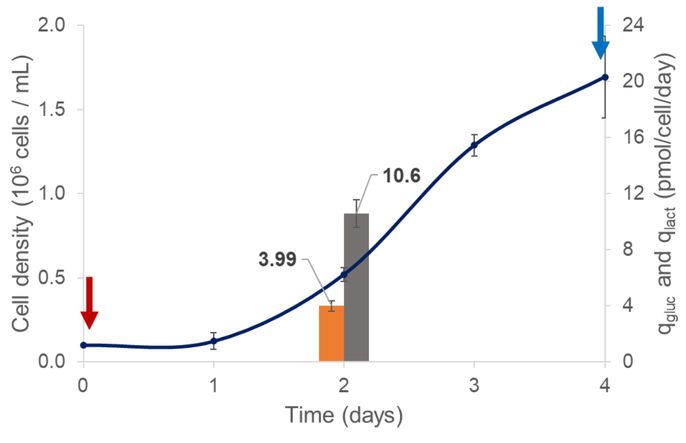

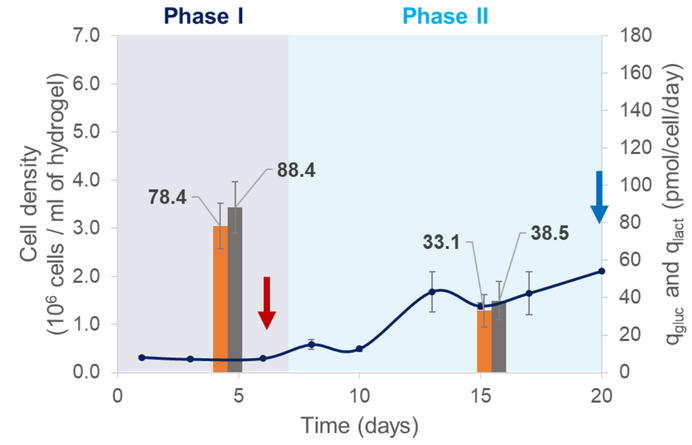

VERO

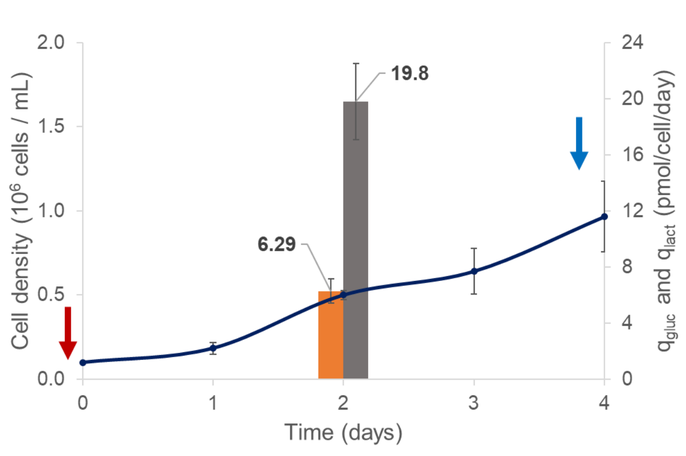

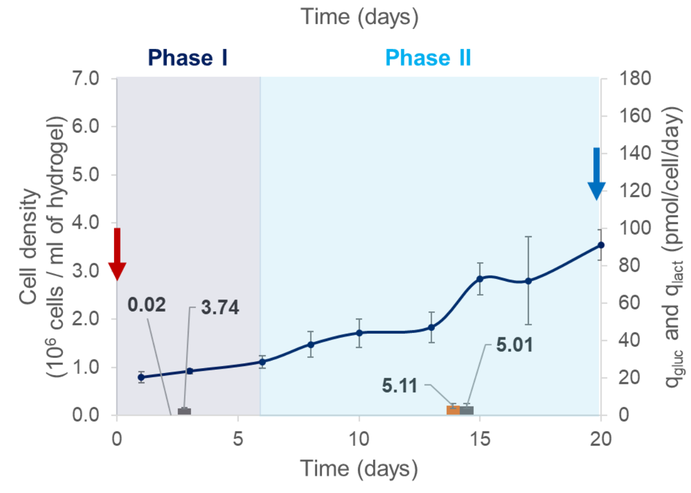

Growth curve

Cell-specific glucose consumption rate : q_{gluc} (pmol/cell/day)

Cell-specific lactate production rate q_{lact} (pmol/cell/day)

Figure 3

Click here to access/download;Figure;Figure 3.pptx

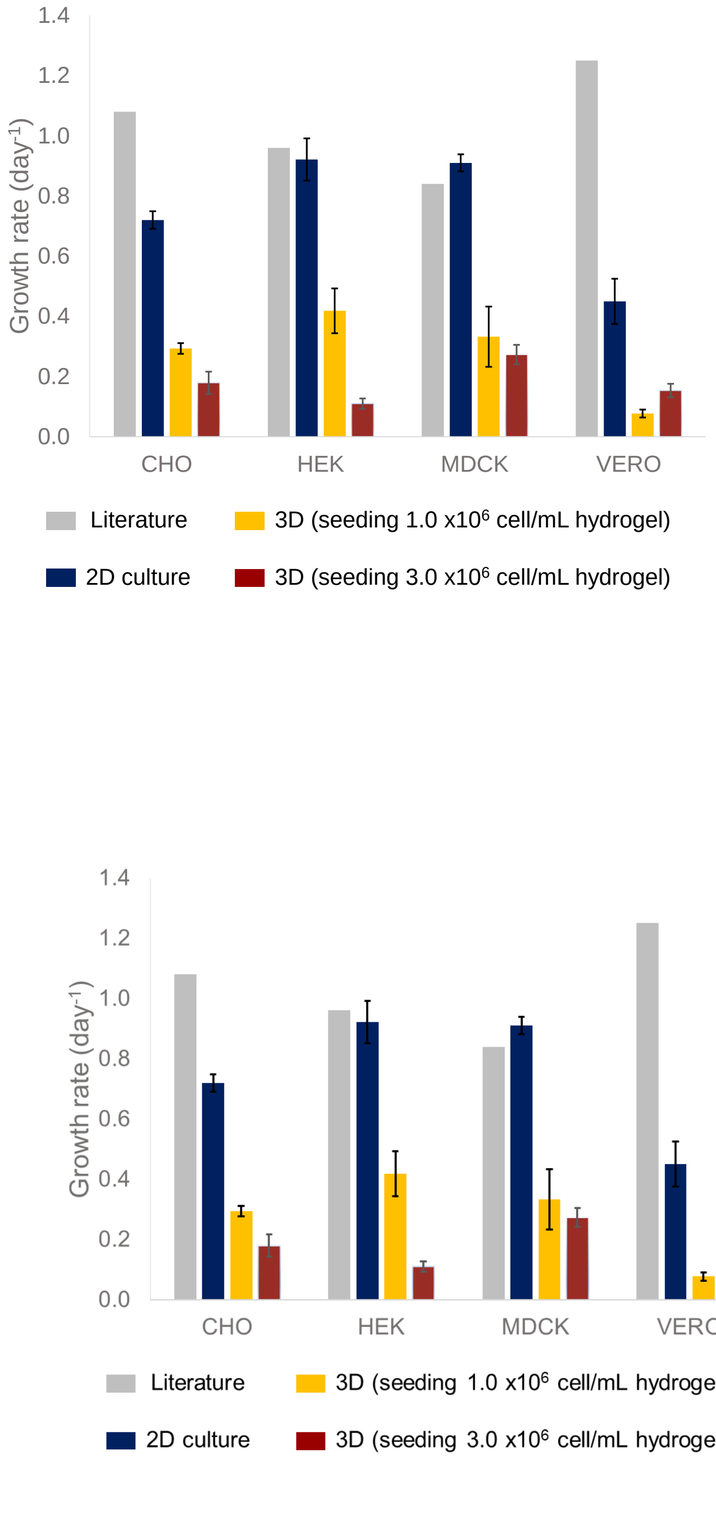

Figure 4

Click here to access/download;Figure;Figure 4.pptx

A

a.1

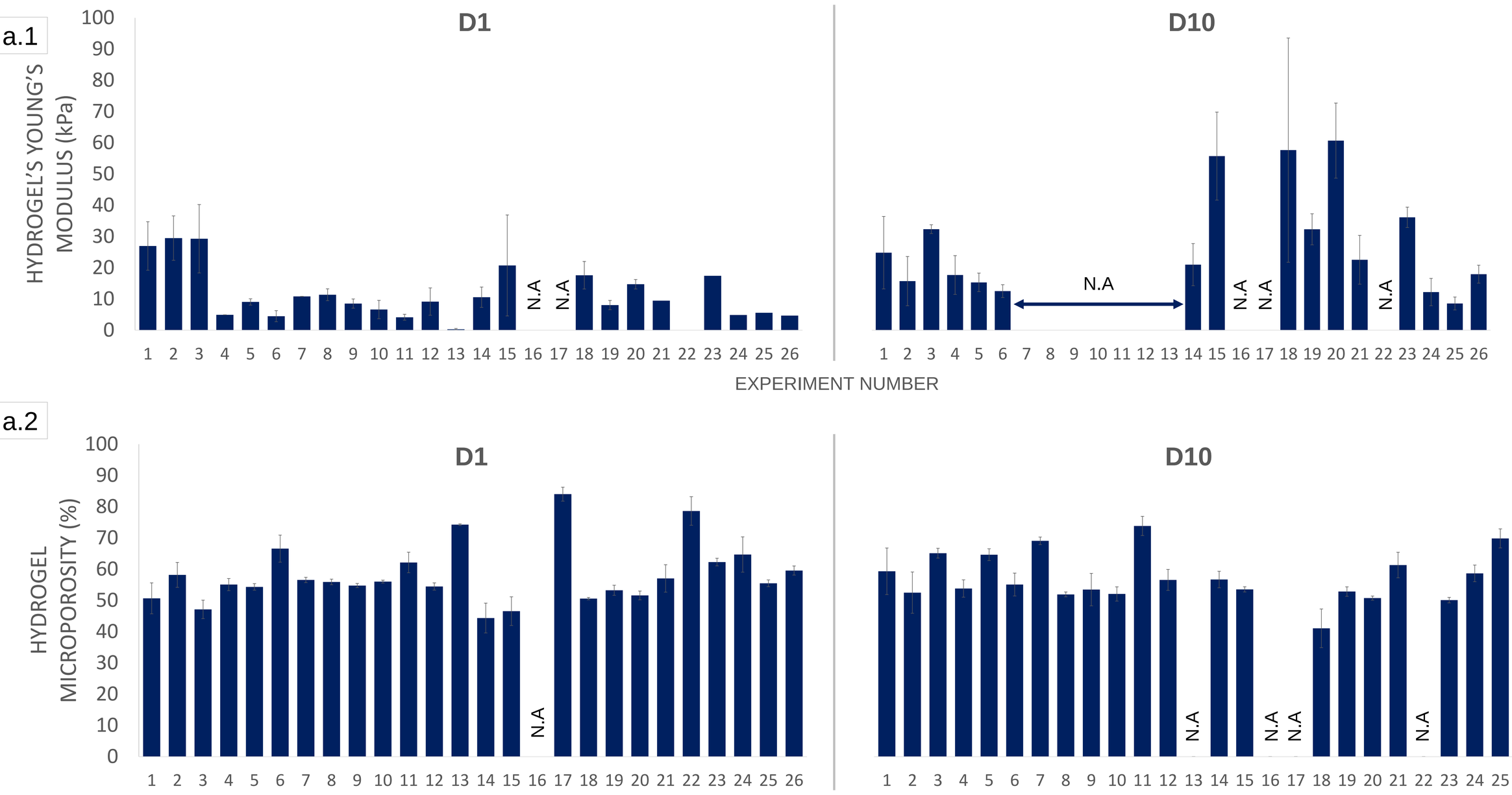

a.2

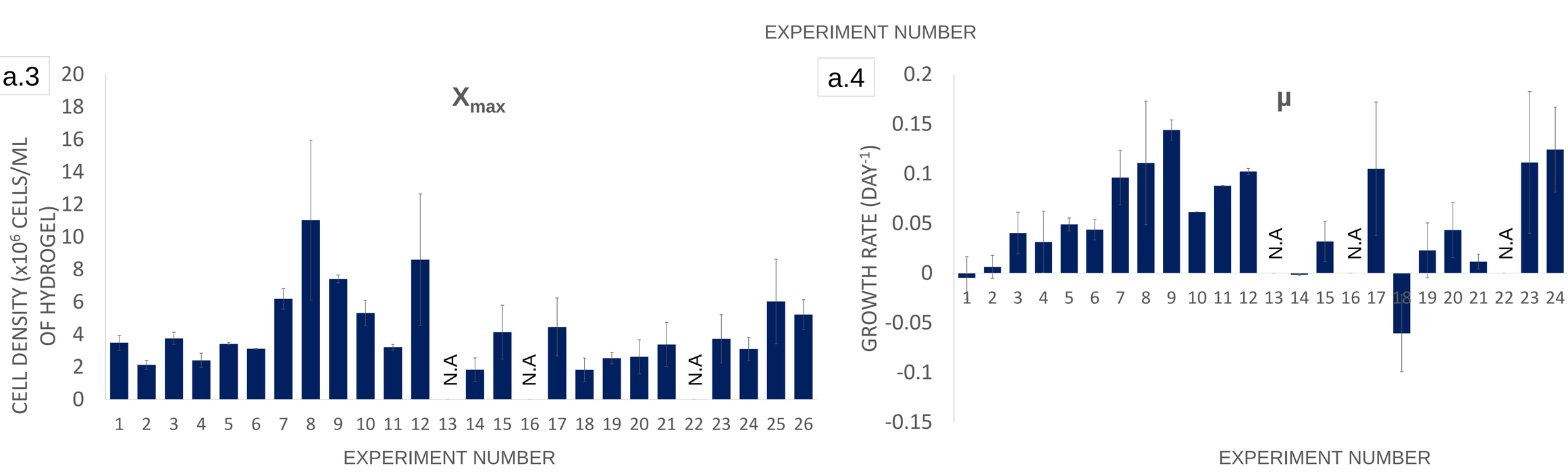

a.3

a.4

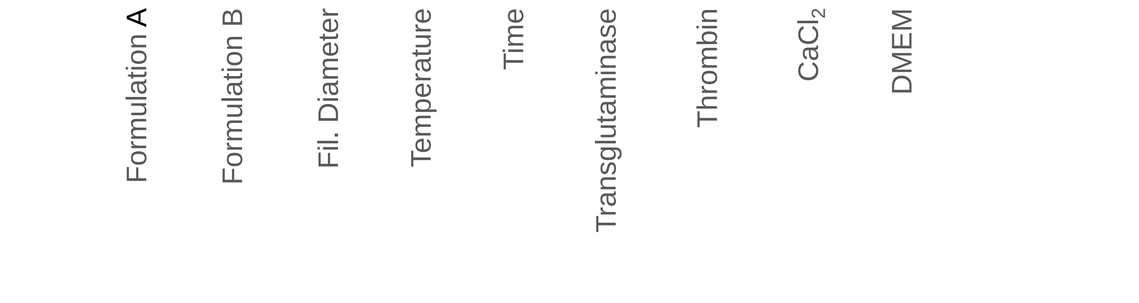

B

b.1

b.2

Supplementary Material 2

Supplementary Material 5

Click here to access/download

Supplementary Material

Supplementary 5.docx

Supplementary Material 8

Emma PETIOT, PhD
Scientist CNRS
Director 3D InnovationLab joint laboratory 3d.FAB / Sartorius
3d.FAB platform
Gembas Team - ICBMS laboratory - Bat Lederer - 1 rue Victor Grignard - Campus LyonTech/la Doua
43, boulevard du 11 Novembre 1918 - BP 82077 - 69 616 VILLEURBANNE Cedex
Phone: (0)6 47 60 59 13

Dear Editor of *Bioprinting*,

I am submitting the manuscript titled “Bioproduction Cell Lines 3D Bioprinting” for consideration in *Bioprinting*. I declare that all authors have disclosed any actual or potential conflicts of interest related to this work.

I confirm the following:

Conflict of Interest: The authors have no financial or personal relationships with other individuals or organizations that could inappropriately influence (bias) our work. Specifically:

- **Financial Interests:** Neither I nor any of the authors have received any funding, honoraria, or paid consulting fees from companies or institutions that could benefit from the results of this study.
- **Institutional Relationships:** The authors have no direct relationships with entities that could be perceived as a conflict of interest in relation to this manuscript.
- **Funding Disclosure:** The research presented was funded by Sartorius. This funding is disclosed in the manuscript acknowledgment section.
- **Affiliations and Involvements:** All affiliations with, or involvement in, any organization with an interest in the outcome of this work have been fully disclosed in the manuscript.

By signing below, I affirm that this disclosure accurately reflects any conflicts of interest related to this manuscript.

Sincerely,

Emma PETIOT